

Flow past in-line oscillating cylinder square cylinder: DNS and linear stability theory

Harshal Suresh Raut



भारतीय प्रौद्योगिकी संस्थान हैदराबाद
Indian Institute of Technology Hyderabad

Department of Mechanical & Aerospace Engineering

June 2016

Declaration

I declare that this written submission represents my ideas in my own words, and where ideas or words of others have been included, I have adequately cited and referenced the original sources. I also declare that I have adhered to all principles of academic honesty and integrity and have not misrepresented or fabricated or falsified any idea/data/fact/source in my submission. I understand that any violation of the above will be a cause for disciplinary action by the Institute and can also evoke penal action from the sources that have thus not been properly cited, or from whom proper permission has not been taken when needed.



(Signature)

(Harshal Suresh Raut)

(ME11B15M000002)

Approval Sheet

This Thesis entitled Flow past in-line oscillating cylinder square cylinder: DNS and linear stability theory by Harshal Suresh Raut is approved for the degree of Master of Technology from IIT Hyderabad



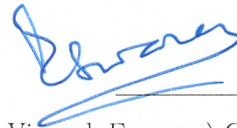
(Dr. Kirti Chandra Sahu) Examiner
Dept. of Chemical Engineering
IITH



(Dr. Chandrika Prakash Vyasarayani) Examiner
Dept. of Mechanical & Aerospace Engineering
IITH



(Dr. H N Dixit) Adviser
Dept. of Mechanical & Aerospace Engineering
IITH



(Prof. Vinayak Eswaran) Chairman
Dept. of Mechanical & Aerospace Engineering
IITH

Acknowledgements

This thesis would not have been possible without the help of two people. The first is my advisor Dr. Harish N. Dixit who provided his constant guidance and support throughout the entire work. He has always motivated to chose the path of research and helped in inculcating the ability of independent thinking. The second person is Dr. Chandrika Prakash Vyasarayani who provided great help in implementing the linear stability analysis code.

I would like to thank my parents as they always supported me for whatever I chose in life and have helped me in achieving my dreams.

Abstract

The thesis consists of two subtopics. The first one includes a numerical study for uniform flow past an inline oscillating square cylinder at Reynolds number of 200. The second one includes linear stability analysis (LSA) of a oscillating wake profile which is obtained by averaging the velocity profile from a flow past a stationary cylinder. The LSA of the oscillating wake profile is done with the aim of obtaining similar vortex shedding structures as obtained from the DNS results for flow past in-line oscillating square cylinder.

The numerical study includes the use of open source software called OpenFOAM [1]. To overcome the limitations with an oscillating inlet flow as used in most of the earlier numerical studies, we prescribed an oscillatory motion for the cylinder in the streamwise direction by using a dynamic meshing feature. After a careful validation of the numerical method which includes reproducing earlier numerical results of lock-on and S-II modes, we systematically carry out a parametric study by varying the amplitude and frequency of oscillation of the cylinder. Two new symmetric modes, named here as S-II-I and S-IV-D have been found. In the S-II-I mode, obtained at large amplitudes and small excitation frequencies of cylinder motion, a pair of vortex dipoles, each of which consists of vortices of unequal strength, are shed from each side of the cylinder in every oscillation cycle but the weaker vortex dissipates quickly resulting in a stable symmetric S-I mode downstream of the cylinder. In the case of S-IV-D mode, obtained at small amplitudes and large excitation frequencies, two pairs of vortex dipoles are shed on either side of the cylinder in every oscillation cycle but these modes quickly dissipate downstream leaving a symmetric streak of vorticity across the centreline. A vortex flapping mode has also been obtained computationally for the first time. In this mode, the vortices arrange themselves in a zig-zag pattern similar to the classical Kármán vortex street, but the entire pattern oscillates about the centreline sinuously. The characteristics of this mode resembles a ‘beating phenomenon’ obtained by interference between two oscillators with slightly differing frequencies. As in most nonlinear oscillators, vortex shedding becomes chaotic when forced sufficiently strongly and is usually associated with nonlinear interactions between competing frequencies. Many of the modes

observed in the current study become chaotic when the peak cylinder velocity (product of amplitude and frequency of motion) becomes comparable to the inlet velocity. We also observe chaos due to mode competition when shedding transitions from an antisymmetric to symmetric modes.

It has been found that the flow past stationary cylinder leads to anti-symmetric vortex pattern. But its also observed that when the cylinder is oscillated in-line with the flow, it can lead to symmetric, anisymmetric or chaotic type of vortex shedding. The linear stability analysis of a steady cylinder wake profile shows the occurrence of antisymmetric vortex shedding pattern on superimposing the mean vorticity and perturbed vorticity contour plots. A preliminary stability analysis using floquet theory is also discussed in the thesis.

Contents

declaration	ii
certificate	ii
Acknowledgements	ii
Abstract	iii
1 Introduction	1
1.1 Scope of the thesis	4
2 Direct Numerical Simulations	6
2.1 Formulation and numerical approach	6
2.2 Validation	9
2.3 Results	13
2.3.1 Symmetric Mode-I (S-II-I)	13
2.3.2 Symmetric Mode-II (S-IV-D)	19
2.3.3 Effect of frequency on S-IV-D mode	20
2.3.4 Effect of Reynolds number on S-IV-D mode	24

2.3.5	Vortex flapping mode	24
2.3.6	Vortex dipole mode (S-II-A-II)	27
2.3.7	Effect of varying amplitude at a fixed excitation frequency	27
2.3.8	Chaotic modes	33
2.3.9	Ambiguous mode	35
2.4	Conclusion	36
3	Linear Stability Analysis	39
3.1	Analysis	39
3.1.1	Formulation	39
3.1.2	Expansion Functions	41
3.1.3	Galerkin Equation	41
3.1.4	Floquet Theorem	42
3.2	Results	43
3.3	Conclusion	46
4	Future Outlook	47
5	Appendix-1	48
6	Appendix-2	57
7	Appendix-3	59

Chapter 1

Introduction

The study of vortex-induced vibrations (VIV) is an area of active research with many open questions of fundamental and applied nature. Vibrations of pipes in heat exchangers and civil engineering structures due to hydrodynamic loads have been extensively studied. Structural failure may result from synchronisation between the fluid excitation force and natural frequency of the system. This hydrodynamic load can sometimes lead to motion of the structure in the streamwise direction [2, 3]. The problem of streamwise oscillation could be particularly severe when a lightly damped cylindrical structure is used in liquids of high density such as water, oil and metal at high temperatures. Such studies have also found application in tracking of underwater bodies.

The failure of Tacoma Narrows Bridge is an excellent example of vortex induced vibration(VIV). The original Tacoma Narrows Bridge roadway twisted and vibrated violently under 40 miles per hour winds on the day of the collapse. Figure 1.1 shows the bridge on the day of collapse.

It is known that flow past stationary bluff bodies leads to antisymmetric vortex shedding behind the body called the Karman vortex street. In this case, the vortices arrange themselves in a zig-zag pattern of alternating strength. But it has been observed in experiments [4, 5, 6, 7, 8] that inline oscillations of the body can lead to variety of antisymmetric,

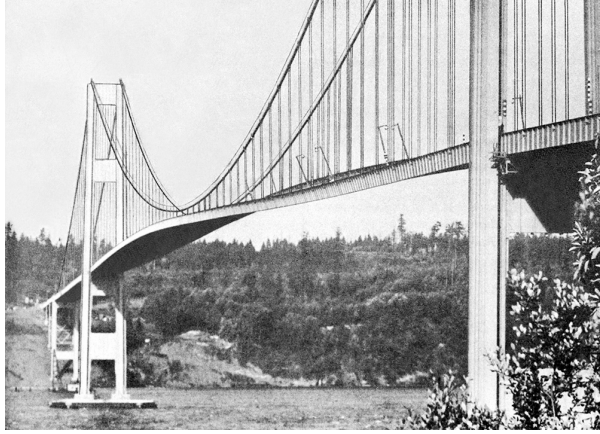


Figure 1.1: Figure showing the Tacoma Narrows Bridge on the day of collapse

symmetric or even chaotic modes of vortex shedding. Symmetric modes of shedding have also been observed in numerical simulations [9, 10, 11], but to the best of our knowledge, all simulations rely on using an oscillating inlet rather than oscillate the body. If the inlet velocity is modulated in a periodic fashion, then it is essential that the minimum velocity in a given time period is also kept positive to preserve the nature of the inlet and outlet boundary conditions. To circumvent this difficulty in the present study, we let the cylinder oscillate in the streamwise direction keeping the inlet velocity fixed. This is enabled by the use of a dynamic meshing feature. To simplify the complexity in mesh generation and mesh motion, we use a square cylinder for the present study. Nevertheless, we expect the results presented in this paper to be valid for cylinders of other shapes.

Among the various studies done on flow past inline oscillating circular cylinder, Griffin and Ramberg[2] were among the first to carry out a systematic experimental study. They found that vortex shedding frequency, f_s , locks on to the frequency of cylinder oscillation, f_e , for $1.2 < f_e/f_o < 2.5$, where f_o is the natural vortex shedding frequency when the cylinder is held stationary. Ongoren and Rockwell[5] in the second of a two part paper on vortex formation behind cylinders of various cross section, discussed their experiments on a cylinder oscillating at an angle α , where $0^\circ \leq \alpha \leq 90^\circ$, relative to the incoming flow. They classified different basic modes of vortex formation on the basis of symmetry, vortex structure, wavelength between two shedding patterns and whether a single vortex or a pair of vortices are observed on the two sides of the wake. In brief, they observed one

400symmetric (called S-I) and four antisymmetric wake patterns behind a circular cylinder.

Konstantinidis & Balabani[7] in their experimental study also noted the S-I symmetric mode as noted earlier by Ongoren and Rockwell[5] wherein one vortex is shed from each side of the cylinder, opposite in sign to the vortex shed from the other side. Xu *et al.* [6] performed experimental studies and discovered a new mode of symmetric shedding called S-II wherein two vortices of opposite sense were shed from each side of the cylinder. Later, the S-II mode was obtained numerically by Srikanth *et al.* [10] in their study of flow past inline oscillating rectangular cylinder.

Apart from symmetric and antisymmetric shedding there has also been evidences of chaotic shedding. Chaotic shedding in flow past inline oscillating circular cylinder was reported by Vittori and Blondeaux[12] and Perdikaris *et al.*[13]. The former study had no mean flow and showed that route to chaos is quasi-periodic whereas the later study gave the reason of mode competition for the occurrence of chaos. The evidence of chaos due to mode competition was then provided by Srikanth *et al.*[10]

Though all the experiments reported above deal with a cylinder oscillating in a constant inlet flow, numerical challenges associated with moving a cylinder have restricted almost all numerical studies to the case of stationary cylinders with an oscillating inlet flow. Consider an inlet with an oscillating velocity given by

$$U_i = U_m + \Delta U \cos(\omega t),$$

where U_i , U_m and ΔU are the magnitudes of the total, mean and fluctuating velocities at the inlet respectively and ω is the frequency of pulsation. To preserve the nature of the boundary condition at inlet and outlet, we require that $\Delta U \leq U_m$. This restricts the range of fluctuating velocities that can be studied in such computations. To overcome this difficulty, we have chosen to carry out simulations with a cylinder oscillating in a uniform inlet. This is perhaps the first systematic study for in-line oscillating cylinders where the cylinder is in motion. We use the open source CFD code *OpenFOAM*[1] with the dynamic

meshing feature for all the computations reported here. Alternately, it is also possible to use vortex blob methods[14] for such computations , but the ease of usage and excellent functionality of *OpenFOAM*[1] prompted us to use the latter.

For all the simulations reported in this paper, we keep the Reynolds number based on the mean velocity fixed at 200. This Reynolds number is large enough for strong vortex shedding patterns to emerge in a flow yet small enough to keep the dominant features of the flow two-dimensional. Hence all the simulations reported in this paper are two-dimensional in nature. We have carried out an extensive parametric study involving over 100 simulations varying the amplitude of the cylinder motion and its frequency. Three new shedding modes are discovered in this study and the results are summarised in the form of a ‘phase-diagram’ in the amplitude-frequency plane. In addition, to the best of our knowledge, a vortex flapping mode has been obtain computationally for the first time.

It has been found that the flow past stationary cylinder leads to anti-symmetric vortex pattern. But it is observed that when the cylinder is oscillated in-line with the flow, it can lead to symmetric, anisymmetric or chaotic type of vortex shedding. The linear stability analysis of a steady cylinder wake profile shows the occurrence of antisymmetric vortex shedding pattern on superimposing the mean vorticity and perturbed vorticity contour plots. The aim of this research is to perform the same type of stability analysis for oscillating wake profile using Floquet Theorem to give the prediction of the mode obtained from the DNS results by varying the amplitude and frequency of the oscillating wake. Similar kind of stability analysis was done by Kerczek and Davis[15] and Grosch and Salwen[16]. Grosch and Salwen[16] did it for plane-poiseuille flow whereas Kerczek and Davis[15] did it for oscillatory stokes layer.

1.1 Scope of the thesis

The entire thesis consists of two different problems. The chapter 2 of this thesis deals with the Direct Numerical Simulations that are performed in OpenFOAM. The chapter 3 of this

thesis includes the Linear Stability Analysis study done with the help of MATLAB. The chapter 4 includes the conclusion that were drawn from the two studies.

Chapter 2

Direct Numerical Simulations

2.1 Formulation and numerical approach

All the numerical simulations have been performed in *OpenFOAM v2.3.0*, a free open source CFD software [1] containing a variety of solvers to simulate a wide variety of flows. The solver used for the present simulations is *pimpleDyMFoam*. *pimpleDyMFoam* is an extension of the *pimpleFoam* solver that allows for dynamic meshes. The solver is transient, allows for relatively large time steps and uses a hybrid PISO-SIMPLE algorithm. Throughout the simulations Courant number is restricted to 0.5 and an adaptive time stepping scheme is employed. We have used the in-built mesh generation tool in OpenFOAM.

To study effect of in-line oscillations of the cylinder, we prescribe a harmonic motion for the cylinder in the direction of the incoming flow. If x_0 is the mean position of the cylinder and $x_b(t)$ is the time variation of the cylinder location, we prescribe

$$x_b(t) = x_0 + A \sin(\omega t), \quad (2.1)$$

where A is the amplitude and $\omega = 2\pi f_e$ is the circular frequency of motion. Differentiating the above equation with time, the velocity of the cylinder, $U_b(t)$, in the direction of the flow

is given by

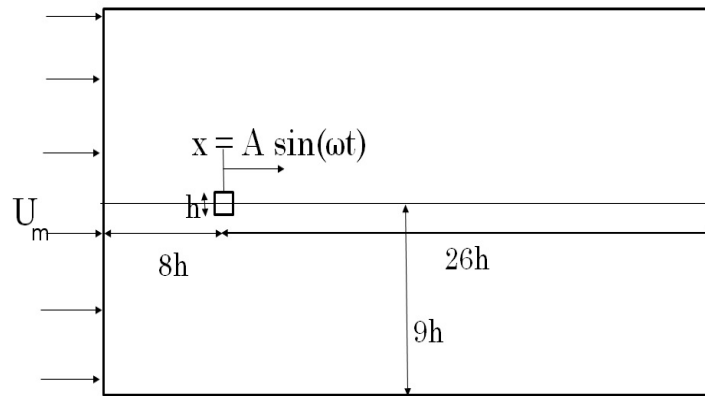
$$U_b(t) = A\omega \cos(\omega t), \quad (2.2)$$

At the inlet, we prescribed a constant uniform flow, U_m . For $A\omega < U_m$, the maximum cylinder velocity is less than the inlet flow and relative velocity between incoming flow and cylinder is expected to be positive at all times. Whereas for $A\omega > U_m$, for a certain duration of each time period, the net relative velocity between the incoming flow and the cylinder is negative, i.e. the cylinder is moving counter to the incoming flow in absolute sense. This regime cannot be simulated in the usual way with a stationary cylinder and an oscillating inlet since prescribing a negative velocity at the inlet leads to numerical complications. The present study is the first numerical study to investigate this regime.

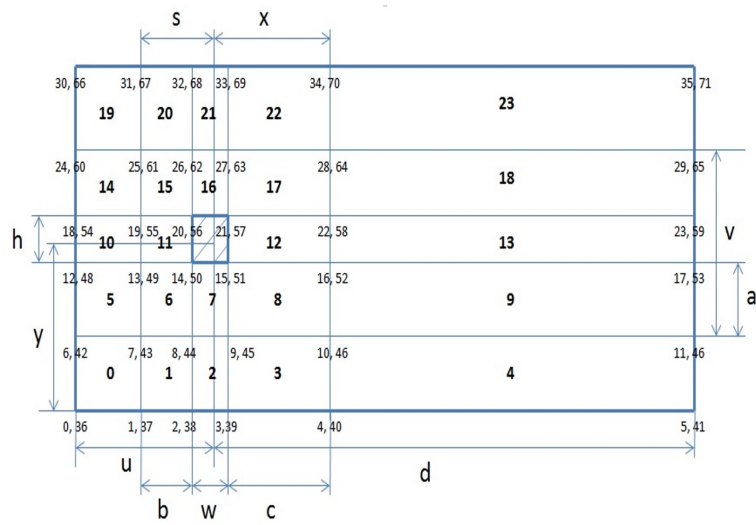
The non-dimensional parameters involved in our simulations are Reynolds number (Re), aspect ratio of the cylinder which is the ratio of height of the cylinder to that of the width of the cylinder, frequency ratio which is the ratio of forcing frequency of oscillating cylinder to that of vortex shedding frequency of stationary cylinders at same Reynolds number, (f_e/f_o), and amplitude ratio which is the ratio of amplitude of oscillating cylinder to that of height of the cylinder, (A/h). In our simulations, we have kept the Reynolds number constant at 200 and aspect ratio at 1. The f_o value that we obtain from our simulation for stationary cylinder at Reynolds of 200 was 0.15204. This matches the Strouhal number value given by [3] for square cylinder at Reynolds number of 200 (with $h = 1$ and $U_m=1$ that we used in our simulations).

Figure 2.1(a) shows the domain used for the simulations, h stands for height of the cylinder and all dimensions are characterised in terms of h . The size of the domain is $34h \times 18h$ with nonuniform grids of up to nearly 150,000 grid points, whose arrangement is shown in figure 2.1(c). To capture the velocity gradients accurately for precise quantification of drag and lift forces, we use a high-density uniform grid in the vicinity of the cylinder as shown in figure 2.1(d).

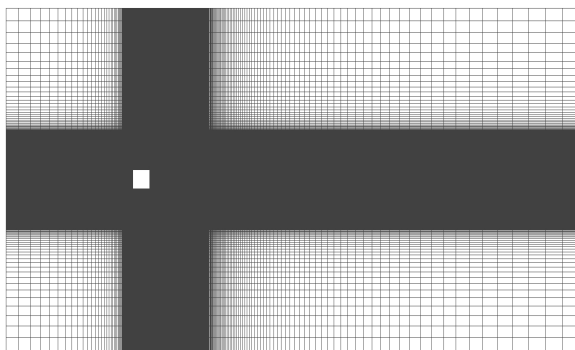
We have used the in-built mesh generation tool in OpenFOAM. From figure 2.1(b) it can be seen that the mesh is divided into 23 blocks. This division is done to ensure that



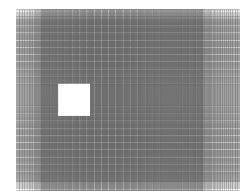
(a)



(b)



(c)



(d)

Figure 2.1: (a) Schematic of the domain used in the simulations along with its dimensions, (b) the grid at the beginning of the simulation, (c) high-density grid in the vicinity of the cylinder.

Table 2.1: Details of the grid dependence test with domain size as shown in Figure 2.1(a)

We have used the in-built mesh generation tool in OpenFOAM. From figure 2.1(b)

Grid size	N_s	f_1	f_2	C_{Dmean}	C_{Lrms}
409 X 370	60	7.573×10^{-2}	0.15146	7.764×10^{-2}	7.061×10^{-3}
475 X 434	70	7.579×10^{-2}	0.1516	7.779×10^{-2}	7.124×10^{-3}
Deviation%		0.08	0.08	0.2	0.88

Table 2.2: Details of the domain dependence test for blockage

Blockage(%)	Grid size	f_1	f_2	C_{Dmean}	C_{Lrms}
5.56(H=18)	409 X 370	7.573×10^{-2}	0.15146	7.764×10^{-2}	7.061×10^{-3}
4.16(H=24)	409 X 436	7.566×10^{-2}	0.1513	7.741×10^{-2}	7.077×10^{-3}
Deviation%		0.088	0.088	0.29	0.224

there is finer mesh near the cylinder and courser mesh as we move away from the cylinder. Figure 2.1(b) shows only the front side of the mesh in which the vertex are numbered from 0 to 35. The rest of the vertices are in the back plane and are numbered from 36 to 71. For more info on mesh generation refer to Appendix 1.

In order to incorporate dynamic meshing two new files needs to be incorporated in the normal OpenFOAM directories. These files include the pointDisplacement file (in 0 folder) and the dynamicMeshDict file in the constant folder. Refer to Appendices 2 and 3 for more details.

2.2 Validation

The domain size is shown in figure 2.1(a) and the optimal values for grid points in the domain were obtained after extensive validation studies and comparison with existing numerical

Table 2.3: Details of the domain dependence test for downstream distance

Downstream	Grid size	f_1	f_2	C_{Dmean}	C_{Lrms}
26	409 X 370	7.573×10^{-2}	0.15146	7.764×10^{-2}	7.061×10^{-3}
32	427 X 370	7.579×10^{-2}	0.15116	7.779×10^{-2}	7.124×10^{-3}
Deviation%		0.08	0.2	0.09	0.883

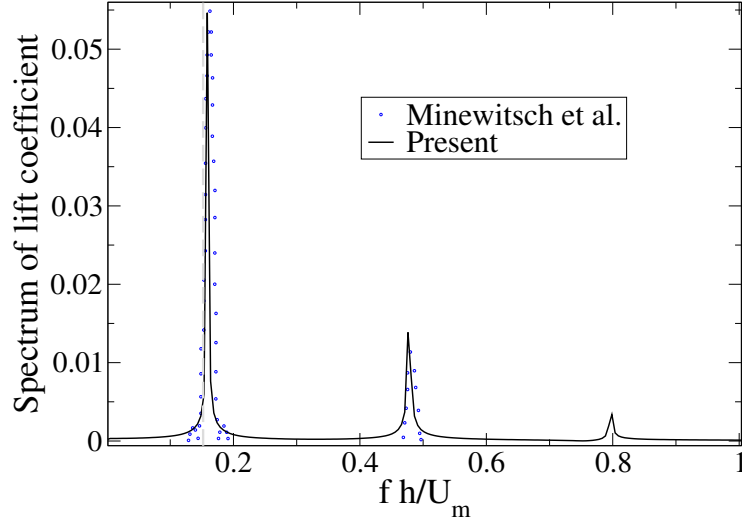


Figure 2.2: Comparison of power spectra of lift coefficient from Minewitsch et al.[17] with our results at $A/h=0.25$ and $f_e/f_0=2$.

results for a stationary cylinder. In the case of an oscillating cylinder, we also carried out a systematic domain and grid independence test. A sample of the key studies is given in tables 2.1, 2.2, 2.3 which shows the results of the grid and domain dependence studies done for $f_e/f_o = 1.5$, $A/h = 0.05$ and $Re = 200$. For grid dependence, the number of grid points on each face of the cylinder, N_s , was varied from 60 to 70. For domain dependence, we separately vary the vertical domain size, H , to study the effect of blockage ratio, table 2.2, and the effect of downstream distance from the cylinder to the outlet boundary, table 2.3. In these tables, f_1 and f_2 indicate the frequencies obtained from the spectra of lift coefficient, C_{Dmean} and C_{Lrms} stands for the mean drag coefficient and root mean square value of lift coefficient respectively. The maximum deviation in the above parameters is well within acceptable limits. Based on these studies a mesh with $N_s = 60$ points on each side of the cylinder and a grid size of 409 X 370 is chosen for all subsequent simulations.

The numerical approach was validated as follows. Strouhal numbers obtained from flow past a fixed square cylinder were found to be in good agreement for a range of Reynolds numbers with the experiments of Okajima[3] and numerical simulations of Ansumali *et al.*[18] We also validated our result with Minewitsch et al.[17] by comparing the power spectrum of lift coefficient at $A/h = 0.25$ and $f_e/f_o = 2$ and is shown in figure 2.2. In all the plots of spectrum of lift coefficient, $(-\cdots-)$ represents f_e and $(---)$ represents f_o . Next,

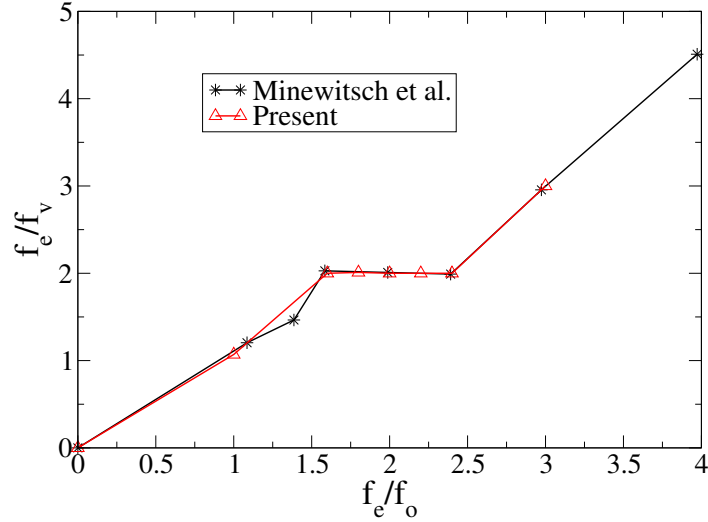
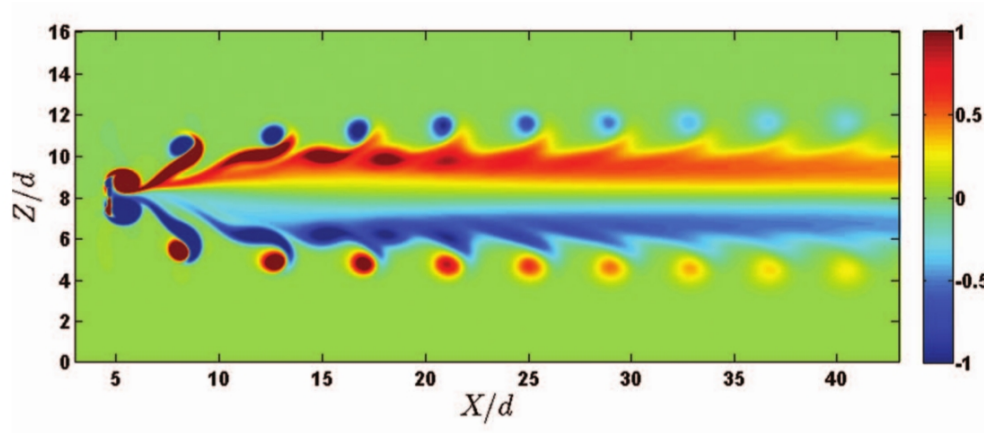


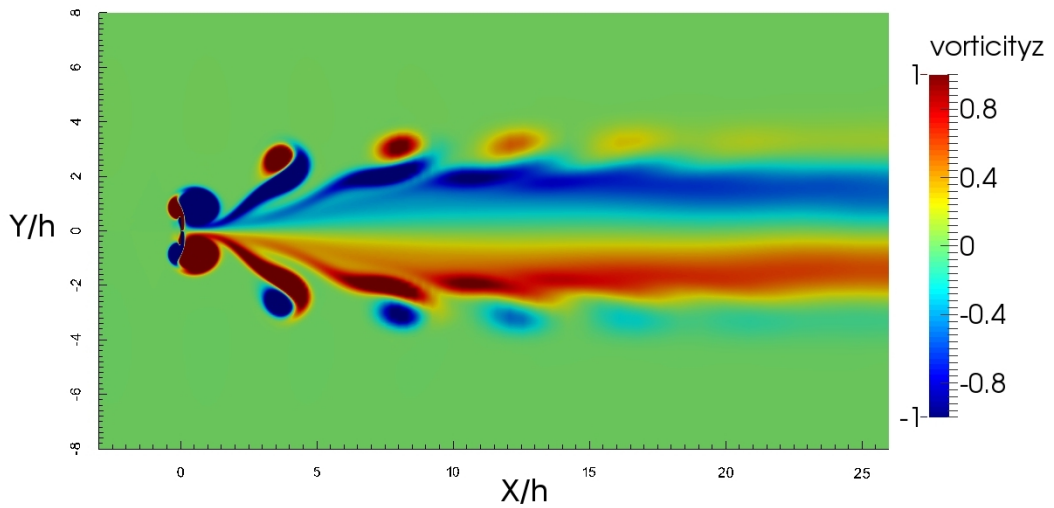
Figure 2.3: Comparison of lock-on phenomenon with Minewitsch et al.[17] for $A/h=0.225$ and $1 < f_e/f_o < 3$.

as done by Minewitsch *et al.*[17], the amplitude ratio was kept fixed at $A/h = 0.225$ and frequency ratio, f_e/f_o , was varied from 1 to 3. The lock-on window between $1 < f_e/f_o < 3$ with $f_v = 0.5f_e$, where f_v is the vortex shedding frequency for an oscillating cylinder, is in excellent agreement with Minewitsch *et al.*[17] as shown in figure 2.3.

To further gain confidence on the numerical procedure, we also reproduce the S-II mode obtained in Khaledi et al.[11] simulating flow past an oscillating thin plate of aspect ratio of 50 and with the same parameters mentioned in Khaledi *et al.*[11]. The simulation is carried out at $A/h = 0.5$ and $f_e/f_o = 1.74$ and results are compared in figure 2.4. It has to be noted that the direction of vorticity vector in Khaledi *et al.* is opposite to that used in the paper. In spite of the larger domain used in Khaledi *et al.*, the vorticity plots agree quite well. Because of a moving grid employed in the present simulations, we use a slightly coarser mesh than Khaledi *et al.* The difference in the sharpness of the two images could be attributed to differing grid densities in the two studies.



(a)



(b)

Figure 2.4: Comparison of S-II mode from Khaledi et al.[11] (a) with our result (b) for $A/h = 0.5$, $f_e/f_o=1.74$ and $Re = 100$ at the same phase. In our case, the cylinder center is at a distance of $8h$ from inlet.

2.3 Results

An extensive parametric study ranging over 100 simulations has been performed by systematically varying the amplitude ratio, A/h , and excitation frequency ratio, f_e/f_o . A summary of all the simulations is shown in the form of a ‘phase-diagram’ in figure 2.5. Neat clusters of similar shedding modes are clearly visible in the plot. It can be observed that the symmetric modes are obtained at either high amplitude-low frequency and high frequency-low amplitude regions. The vortex flapping modes, to be described later, are obtained close to frequency ratio between 0.8 to 1.5. At low amplitude ratios, beyond $f_e/f_o > 3$, the modes appears to become progressively symmetric with increasing amplitude ratio and for $f_e/f_o > 4.25$, a symmetric mode, S-IV-A, is observed. We find that the shedding becomes chaotic as we move close to the line where the peak body velocity, $A\omega$, becomes equal to the inlet velocity, U_m . Recall that $\omega = 2\pi f_e$, thus we have

$$2\pi f_e A = U_m \implies \left(\frac{A}{h}\right) \left(\frac{f_e}{f_o}\right) = \frac{U_m}{2\pi h f_o}, \quad (2.3)$$

which is the equation of a rectangular hyperbola as shown in figure 2.5. Chaos is also observed when there is a mode transition from vortex flapping mode to symmetric mode in high amplitude-low frequency region.

therefore

We now present a detailed discussion on the structure and characteristics of various modes of vortex shedding obtained.

2.3.1 Symmetric Mode-I (S-II-I)

Two new symmetric modes have been observed in our simulations. The first symmetric mode represented by the symbol (*) in figure 2.5 is obtained for $f_e/f_o \approx 1$ and moderate values of A/h . The vorticity contours at a particular time and frequency ratio of $f_e/f_o = 0.807$ is shown in figure 2.6 for different amplitude ratios. This mode is similar to the

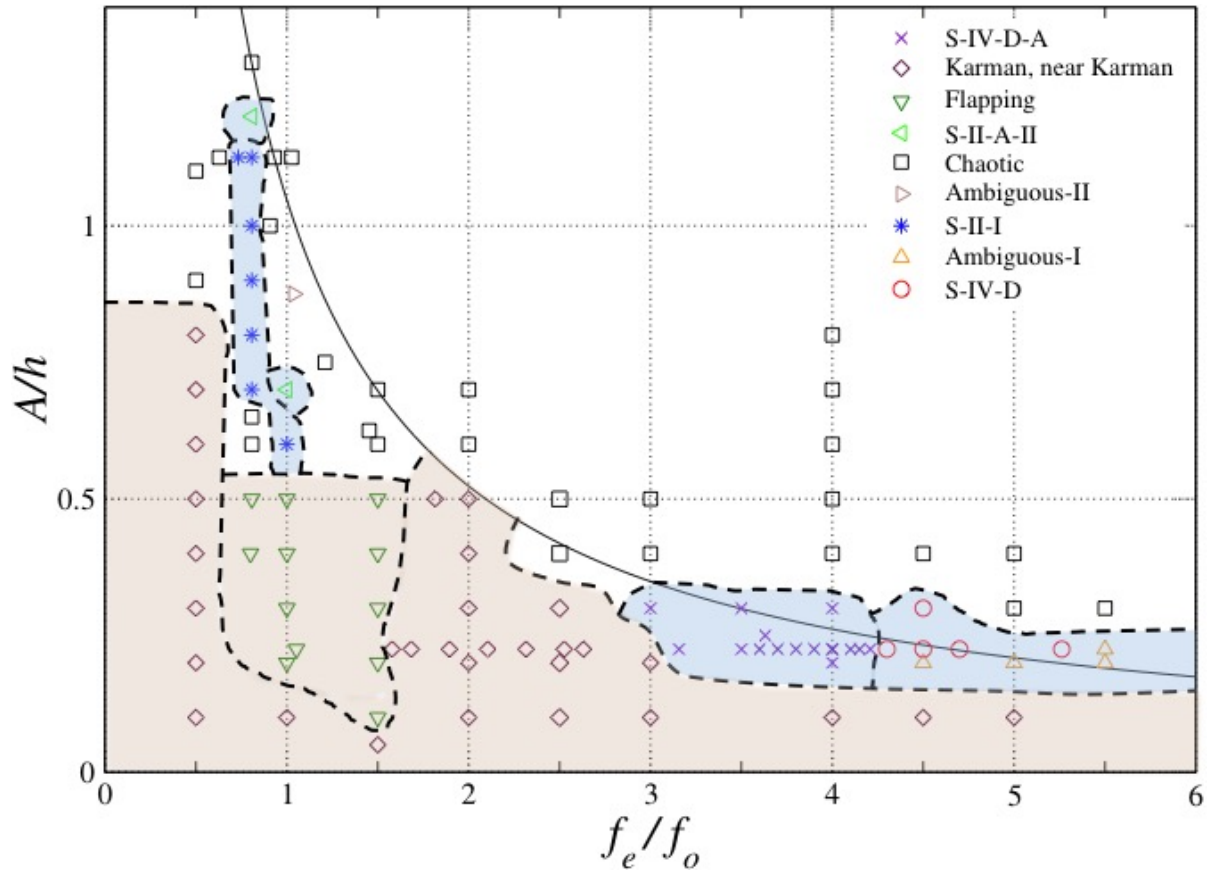
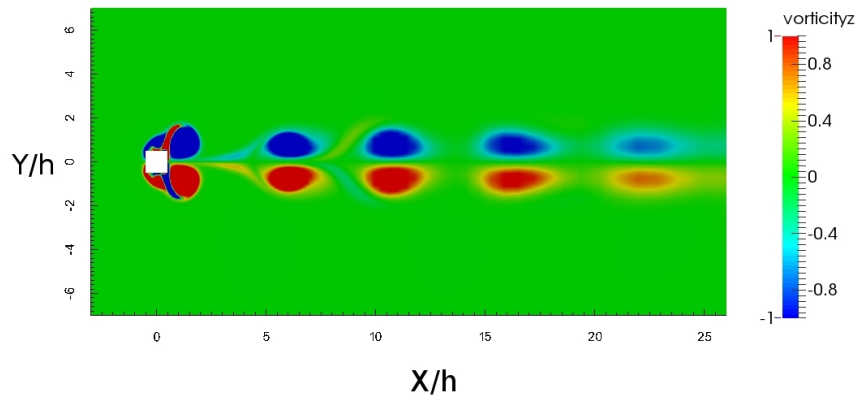
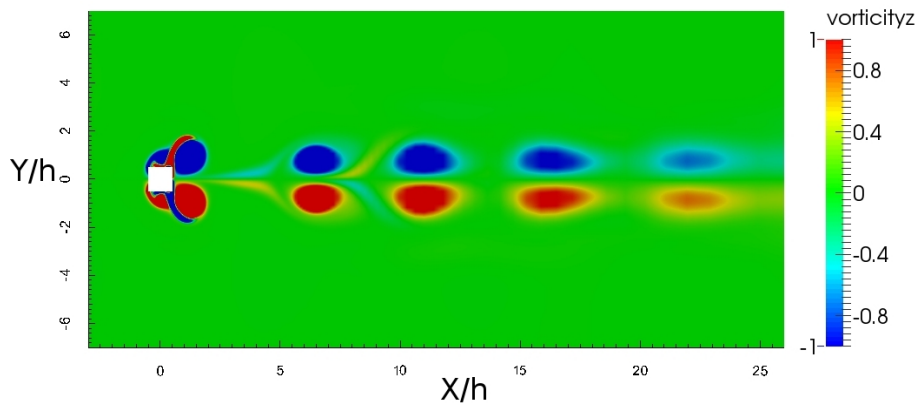


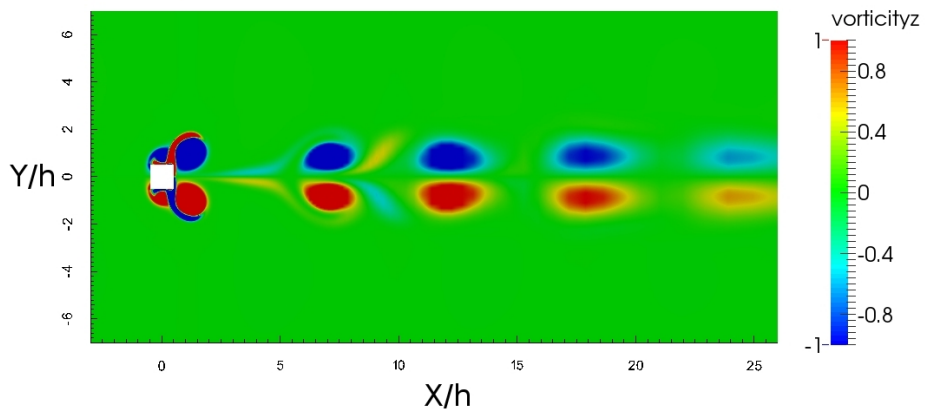
Figure 2.5: A map of various shedding modes obtained by varying frequency, f_e , and amplitude, A of excitation. The solid line is a rectangular hyperbola obtained by equating the inlet velocity with the peak velocity of the body, i.e. therefore, $A\omega = U_\infty$. See text for a detailed discussion of various modes and their nomenclature.



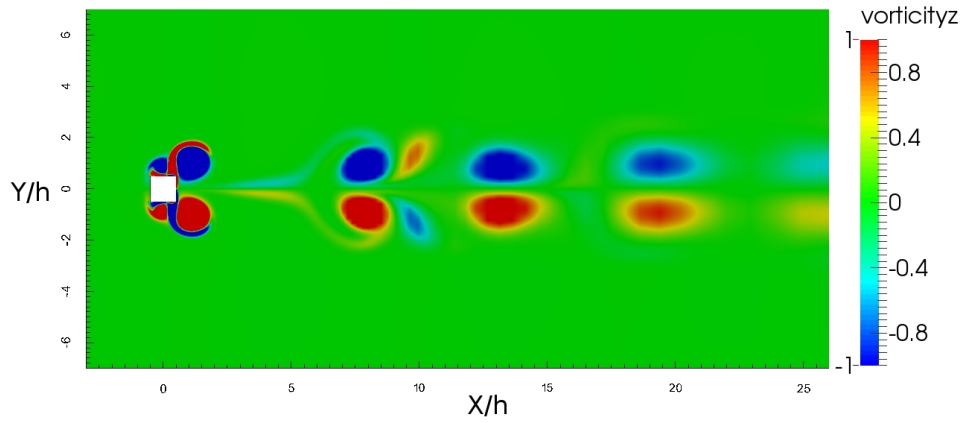
(a)



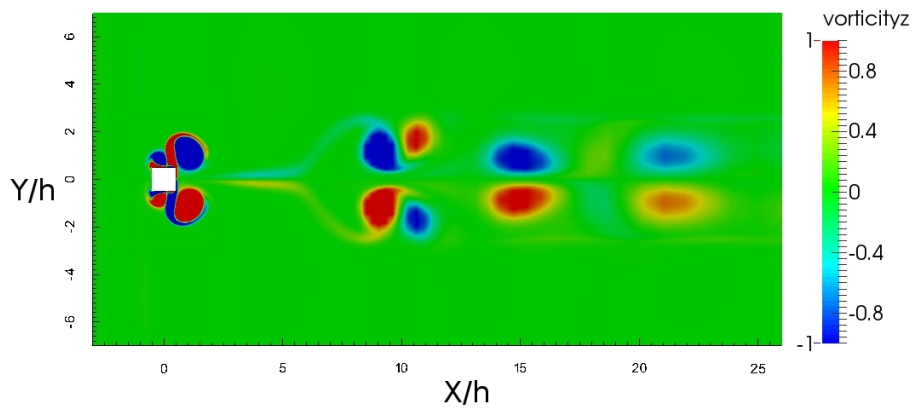
(b)



(c)



(d)



(e)

Figure 2.6: Symmetric mode (S-II-I) obtained at $f_e/f_o=0.807$ and (a) $A/h=0.7$, (b) $A/h=0.8$, (c) $A/h=0.9$, (d) $A/h=1$ (e) $A/h=1.125$. In all cases, the cylinder center is at a distance of $8h$ from inlet.

S-II mode reported earlier by Xu *et al.*[6] in the sense that that two vortices of opposite sense are shed from each side of the cylinder, but the structure of the mode is different in appearance from that reported in Xu *et al.*. In the vicinity of the cylinder, the shedding appears like an S-II mode, but the weaker vortex on each side quickly dissipates downstream of the cylinder and the mode begins to appear like an S-I mode with one vortex on each side of the centreline. The parameters at which this mode appears in the present study was not studied in earlier numerical studies of either Srikanth *et al.*[10] (studied low A/h cases from 0.1 and 0.175) or Minewitsch *et al.*[17] (studied cases with $A/h < 0.4$). This mode seems similar to that obtained by Zhou and Graham[9] for $Re = 600$, $KC = 3$ and $B = 1$ (here, KC stands for Keulegan-Carpenter number which is $U_w T/D$, where U_w is the maximum velocity of oscillation, T is the period of oscillation and D is the diameter of circular cylinder, and B is U_c/U_w , where U_c is the mean stream velocity), but unlike in their case where the flow structure quickly switched to a Karman-type alternating vortex street downstream of the cylinder, here it remains like a stable S-I mode throughout the domain.

In this mode, a pair of primary vortices of opposite sign start to form behind the cylinder as the cylinder moves against the flow. And when the cylinder moves with the flow, another small pair of secondary vortices are created. The primary and secondary vortices form a dipolar vortex pair with the former dominating in strength. As the cylinder reaches its extremum point while moving with the flow, both the vortex pairs detach from the cylinder and form a pair of symmetric dipoles on each side of the centreline creating the S-II mode. Since the secondary vortex is weak, it get sheared away as the vortices travel downstream and thus only the primary vortices on each side of the centreline survive resulting in an S-I mode. We therefore name the combined vortex structures as S-II-I to indicate that two symmetric vortex pairs are shed from the cylinder but a single symmetric pair survives as the structure travels downstream.

The S-II-I mode is formed in a narrow band of frequency ratios and a wider band of amplitude ratios. As is evident from figure 2.6, the the strength of the secondary vortices increase with increasing amplitude. The frequency of vortex shedding is found to be constant

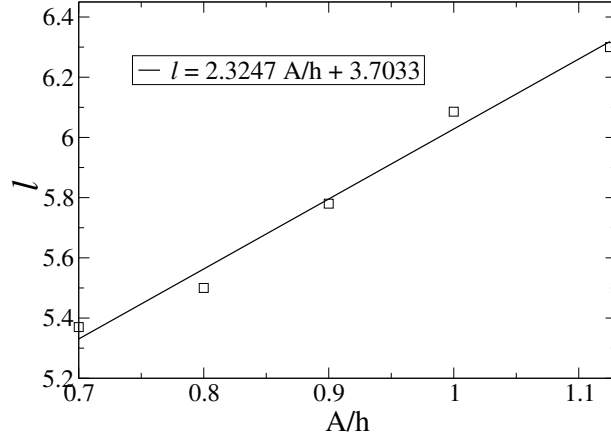


Figure 2.7: Effect of amplitude ratio, A/h , on the spacing between the vortices, l , measured downstream of the cylinder for the S-II-I mode shown in figure 2.6 at frequency ratio $f_e/f_o = 0.807$.

for the cases reported in figure 2.6 and is found to be equal to f_e , i.e. $f_v = f_e$. Since the spacing between successive vortex pairs is proportional to the ‘effective’ flow velocity and inversely proportional to frequency of shedding, we expect

$$l \propto \frac{U_{eff}}{f_v},$$

where $U_{eff} = U_m + \alpha A\omega$ is the effective upstream velocity over one cycle of cylinder motion written in terms of the mean velocity, U_m , at the inlet and a fraction ($0 < \alpha < 1$) of the peak cylinder velocity, $A\omega$. With β as the proportionality constant and using $f_v = f_e$, we get

$$l = \frac{\beta(U_m + \alpha A\omega)}{f_e}, \quad (2.4)$$

The above relation shows that the vortex spacing depends linearly on the amplitude of cylinder motion. In the above expression, α and β can be determined by fitting measured vortex spacing against amplitude ratio A/h . We measure the spacing between the S-I pair of vortices downstream of the cylinder in figure 2.6 and fit a straight line of the form $l = aA + b$ with $a = 2.324$ and $b = 3.703$. This is a least square fit and approximates the data reasonably well as shown in figure 2.7. Comparing the fit to equn. (2.4), we find $\alpha = 0.814$ and $\beta = 0.454$. Thus the effective inlet velocity which produces the S-II-I mode is $U_{eff} = U_m + 0.814A\omega$.

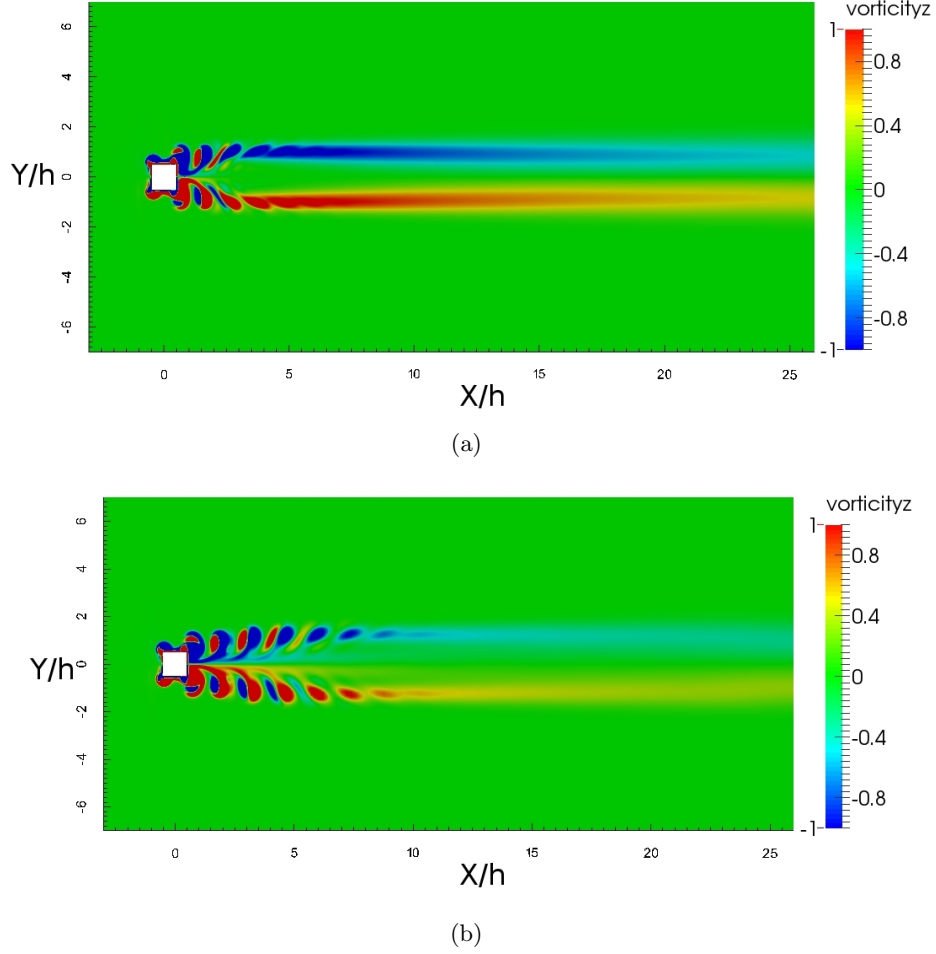


Figure 2.8: S-IV-D symmetric mode obtained with (a) $A/h = 0.225$ and $f_e/f_o = 5.26$ and (b) $A/h = 0.3$ and $f_e/f_o = 4.5$. In our case, the cylinder center is at a distance of $8h$ from inlet.

2.3.2 Symmetric Mode-II (S-IV-D)

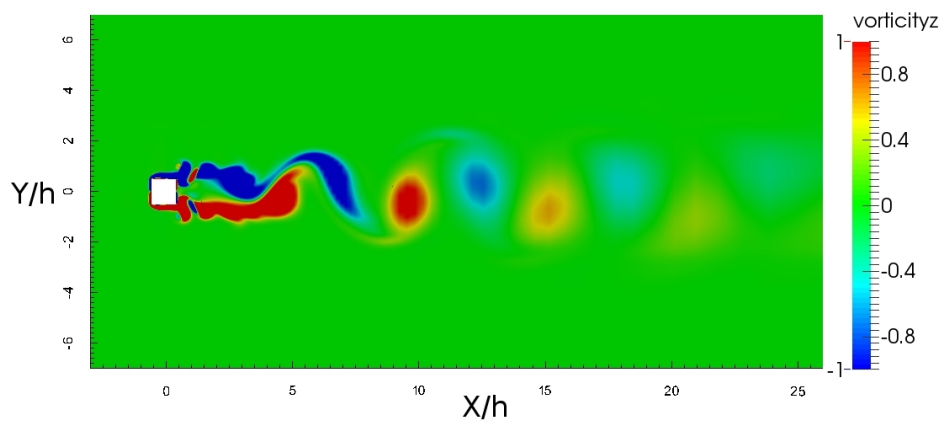
The second symmetric mode, represented by the symbol (\circ) in figure 2.5, is found in the opposite end of the parameter space, i.e., for large f_e/f_o and small A/h . Vorticity plots for two such modes is shown in figure 2.8. This mode has not been reported in earlier results, especially the work of Srikanth *et al.* [10] and Minewitsch *et al.* [17] as their study was restricted to $f_e/f_o < 4$.

Moreover, this mode occurs in the vicinity of the hyperbola in figure 2.5 where $A\omega$ is close to inlet velocity, which is not possible to achieve with an oscillating inlet simulation

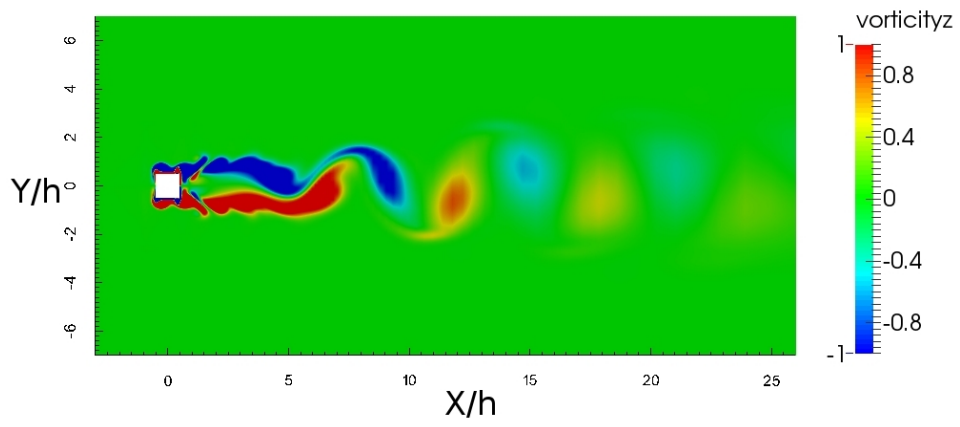
as opposed to a cylinder oscillating in a uniform flow. In this mode two pairs of vortices of opposite sense are being produced on each side of the cylinder across the centreline in one cycle. As the cylinder moves against the incoming flow, a vortex pair on the front and rear side of the cylinder forms symmetrically on the top and bottom side, and as the cylinder recedes in the direction of incoming flow, one vortex out of each vortex pair grows, rolls up and move away while the other spreads out. As a result there are two vortex pairs shed from each side (top and bottom) of the cylinder. This mode can be termed as S-IV but it is different from the S-IV mode obtained by Khaledi *et al.*[11] which was due to splitting of the vortices in S-II mode. The spacing between the vortices is much smaller in this mode, figure 2.8(a), due to the high frequency forcing provided by the cylinder. Intuitively, we expect such high frequency modes to decay rapidly due to viscosity, thus the effect of cylinder oscillation is felt in a narrow region in the downstream direction. We therefore refer to this mode as S-IV-D where S stands for symmetry, IV represents the four vortex pairs shed per cycle and D stands for the vortex decay downstream. It is therefore unsurprising that decreasing frequency ratio increases the extent of the discrete vortical structures as can be seen in figure 2.8(b) for $A/h = 0.3$ and $f_e/f_o = 4.5$.

2.3.3 Effect of frequency on S-IV-D mode

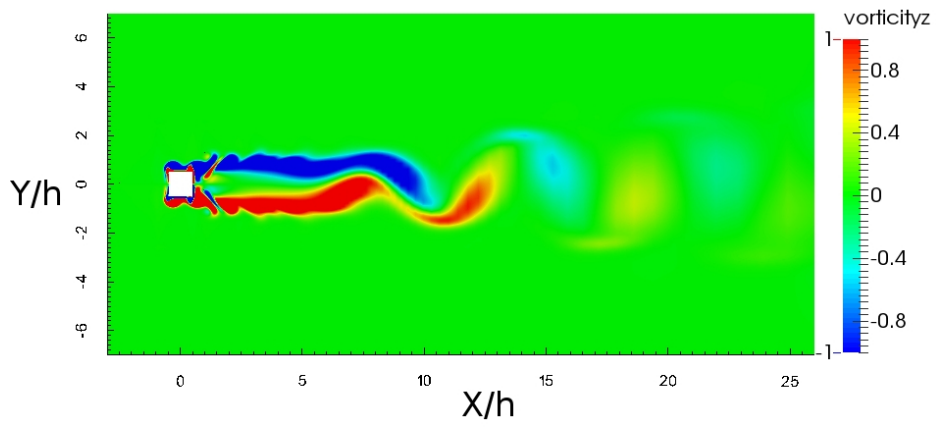
To understanding how the S-IV-D mode emerges from an antisymmetric mode, we fix the amplitude ratio, A/h , at 0.225 and vary the frequency ratio, f_e/f_o from 3.5 to 4.3. At $f_e/f_o = 3.5$ shown in figure 2.9(a), vortex shedding in the vicinity of the cylinder is symmetric even though it quickly disintegrates into an antisymmetric mode downstream. We refer to these intermediate modes with a small antisymmetric structure far downstream with the notation S-IV-D-A where S-IV represents that the shedding in the vicinity of the cylinder is an S-IV mode, D represents decay of vortical structures and A stands for axisymmetric shedding occurring further downstream. The parameters at which these modes emerge is represented by the symbol (\times) in figure 2.5. The symmetric region increases in length with frequency ratio till the entire pattern becomes symmetric, at least within the extent of the domain as shown in figures 2.9(b)-2.9(f). It is unclear at this stage if a true



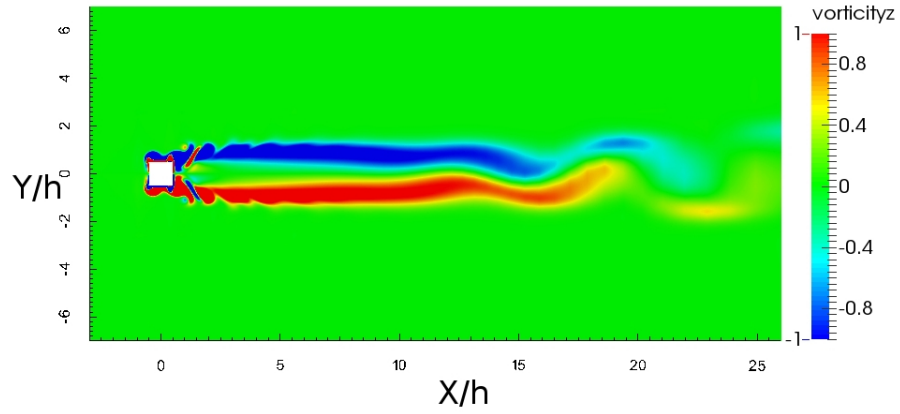
(a)



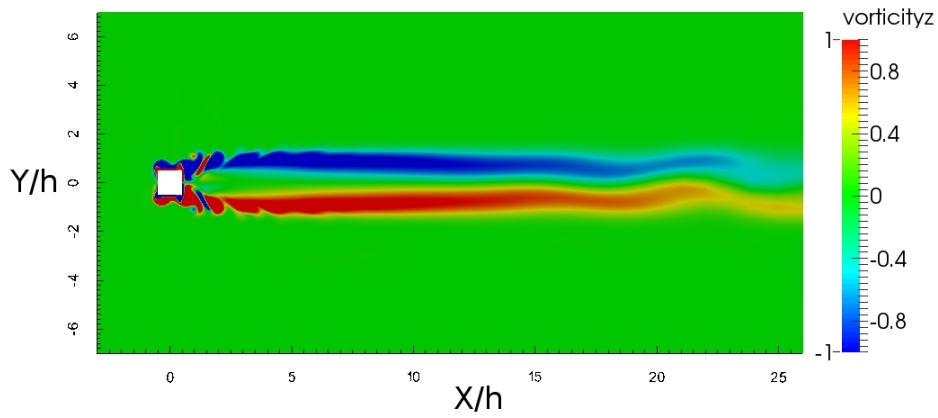
(b)



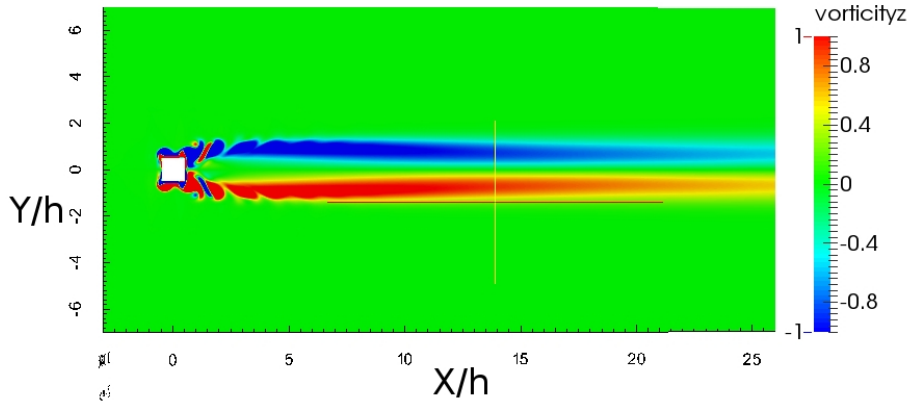
(c)



(d)



(e)



(f)

Figure 2.9: Emergence of the symmetric mode S-IV-D with increasing frequency at a fixed $A/h = 0.225$: (a) $f_e/f_o=3.5$, (b) $f_e/f_o=3.7$, (c) $f_e/f_o=3.9$, (d) $f_e/f_o=4.1$, (e) $f_e/f_o=4.2$, (f) $f_e/f_o = 4.3$. Because of an anti-symmetric region downstream, we call these intermediate modes S-IV-D-A. In all cases, the cylinder center is at a distance of $8h$ from inlet.

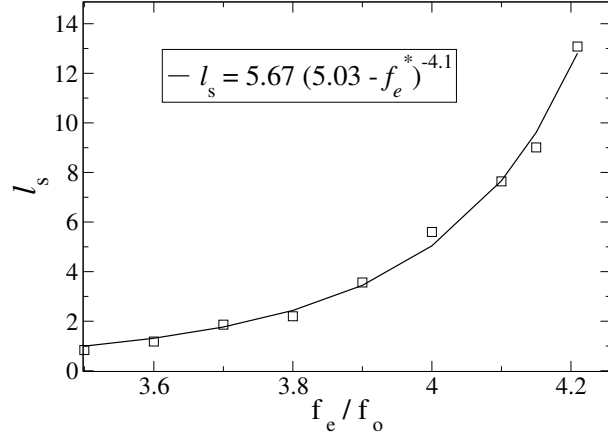


Figure 2.10: Plot between length at which first peak in vertical velocity reaches a value of 1% of U_m along cylinder centreline from cylinder center and frequency ratio (f_e/f_o)

S-IV-D mode would appear if a domain of infinite downstream extent were to be used. To verify this fact, we plot the ‘length’ of the symmetric region, l_s , with frequency ratio. Interestingly, the length follows a power-law with frequency with a negative exponent as shown in figure 2.10. A power-law fit of the form

$$l_s = l_0 (f_c^* - f_e^*)^{-\alpha}, \quad (2.5)$$

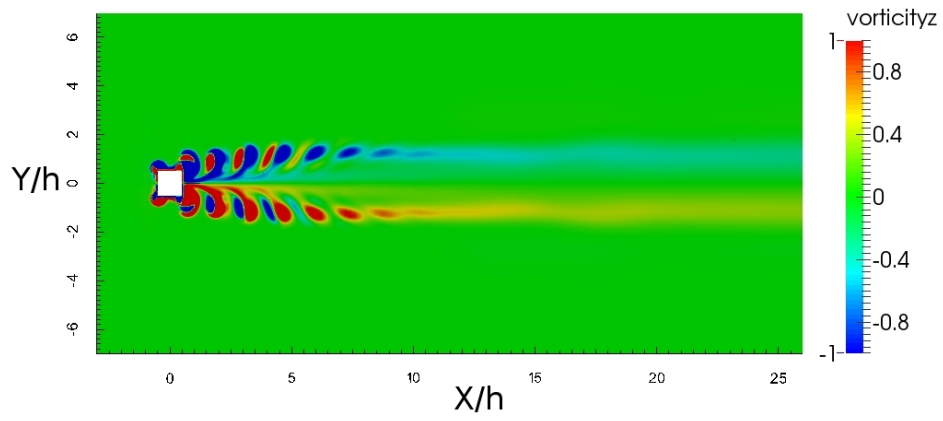
appears to agree well with the numerical data. Here the length l_0 is a numerical pre-factor, $\alpha > 0$, f_c^* and f_e^* are the critical and excitation frequency normalised by the frequency f_o . We refer to f_c^* as the critical frequency as this is the frequency at which the length of symmetric region diverges thus giving us a true symmetric S-IV-D mode even for a domain of infinite extent. Both f_c^* and α are determined by standard curve fitting techniques. The length of the symmetric region is determined as follows: we plot the vertical velocity along the centreline and take l_s to be equal to the length at which the vertical velocity reaches 1% of the mean inlet velocity. It has to be noted that for a perfectly symmetric mode, the vertical velocity, by symmetry, would be identically zero along the centreline. The exact length l_s from this procedure would therefore depend on the cut-off % employed, thus l_0 is not a robust parameter.

2.3.4 Effect of Reynolds number on S-IV-D mode

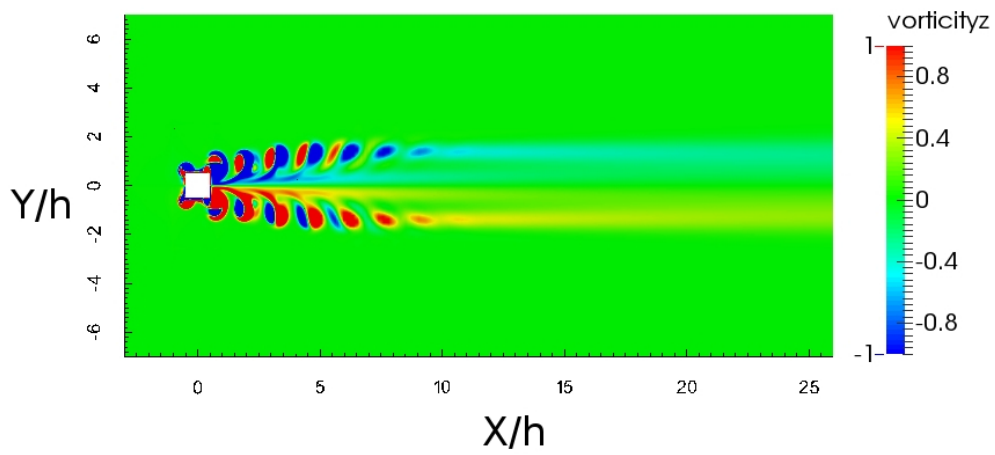
The S-IV-D mode occurring on the lower right part of the parameter space of figure 2.5 has a much finer structure than its other symmetric counterpart, the S-II-I mode occurring at the top left part of figure 2.5. This suggests that the S-IV-D modes are more susceptible to variations in viscosity. The vorticity contours for five different Reynolds numbers, shown in figure 2.11, reveals that the length of the symmetric region (where discrete vortices are visible) increases linearly with Reynolds number as is evident from figure 2.12. The parameters for these plots, slightly different from those of figure 2.9, are $f_e/f_o = 4.5$ and $A/h = 0.3$.

2.3.5 Vortex flapping mode

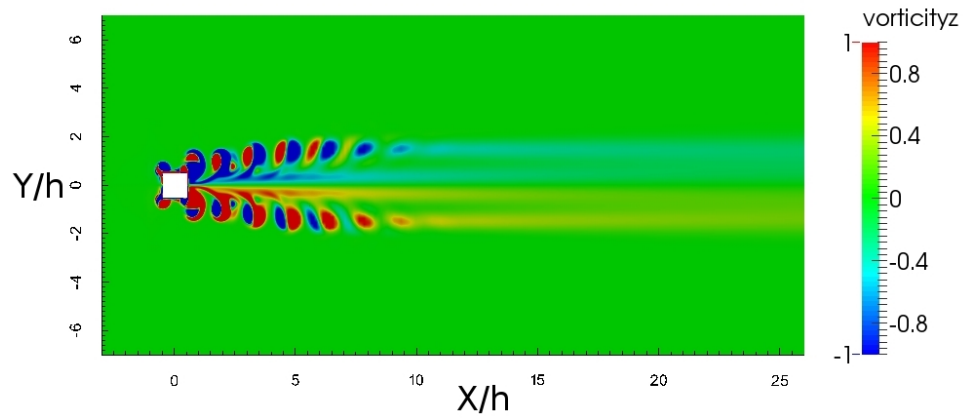
A vortex flapping mode has been found in our simulation for $A/h \leq 0.5$ and $f_e \approx f_o$ and is represented by the symbol (∇) in figure 2.5. The vorticity plot for $A/h = 0.4$ and $f_e/f_o=0.8$ and can be seen in figure 2.13(a). In this mode the vortex street flaps about the centreline of the square cylinder over a time scale much longer than the shedding or excitation time scale. A plot of the lift coefficient with time shown in figure 2.14(a) reveals distinct wave-packet like structures and the frequency spectrum reveals multiple peaks as shown in figure 2.14(b). The frequency is normalised by inertial time scale, h/U_m . A dominant peak appears at f_o and a second peak appears at $|f_o - f_e|$ which is the frequency corresponding to the flapping mode. Using the numerical values of f_o and f_e , the non-dimensional value of the flapping frequency is 0.03 for this particular case. This mode seems similar to the beating string mode obtained by Detemple-Laake and Eckelmann[8] where they obtained it by superimposing vortex shedding with sound waves, but to the best of our knowledge, this mode is obtained numerically for the first time. As $f_e \rightarrow f_o$, the flapping timescale becomes progressively longer and at $f_e/f_o = 1$, the flapping stops and the vortex street tilts to one side of the centreline as shown in figure 2.13(b). It has to be noted that the vortex street settling down on only one side of the centreline for $f_e \rightarrow f_o$ is dictated by factors such as the numerical scheme used for spatial and temporal discretisation, preferential (but tiny)



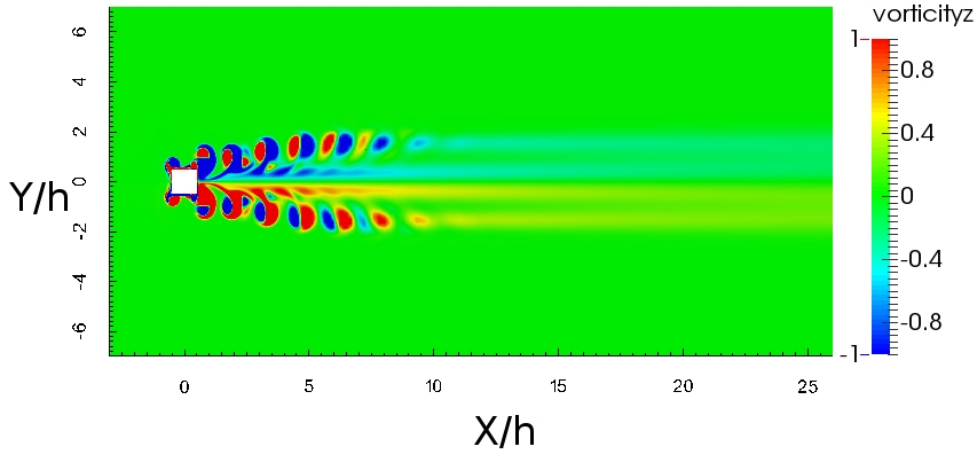
(a)



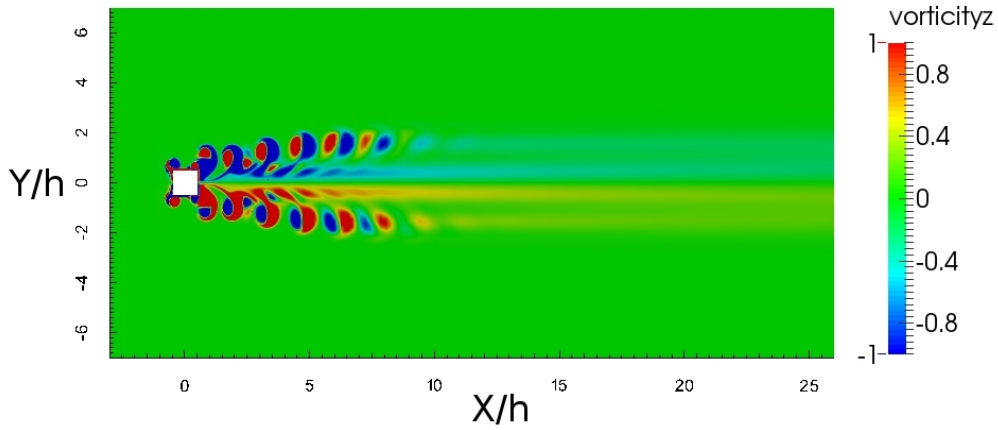
(b)



(c)



(d)



(e)

Figure 2.11: Symmetric mode (S-IV-D) obtained at $A/h=0.3$, $f_e/f_o=4.5$ and (a) $Re=200$, (b) $Re=225$, (c) $Re=250$, (d) $Re=275$, (e) $Re = 300$. In all cases, the cylinder center is at a distance of $8h$ from inlet.

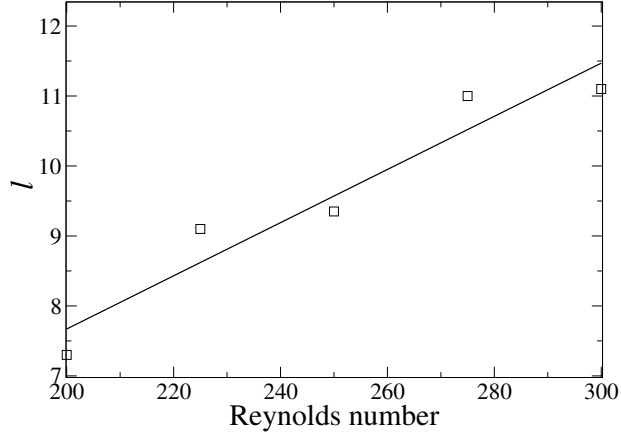


Figure 2.12: Variation of length of symmetric S-IV region near the cylinder with Reynolds number. The length, l , corresponds to the downstream distance from the cylinder where discrete vortex blobs appear. The solid line is a straight line fit to the numerical data obtained with a fixed $f_e/f_o=4.5$ and $A/h = 0.3$.

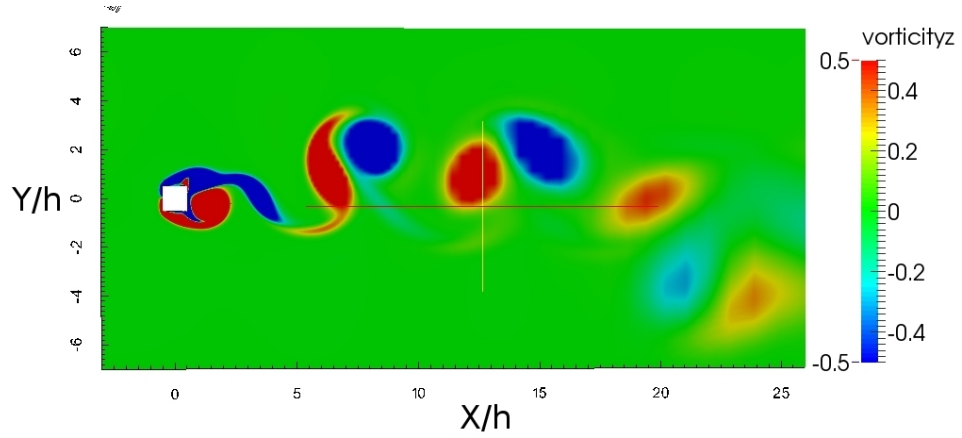
accumulation of numerical errors over the course of the numerical simulation, etc.

2.3.6 Vortex dipole mode (S-II-A-II)

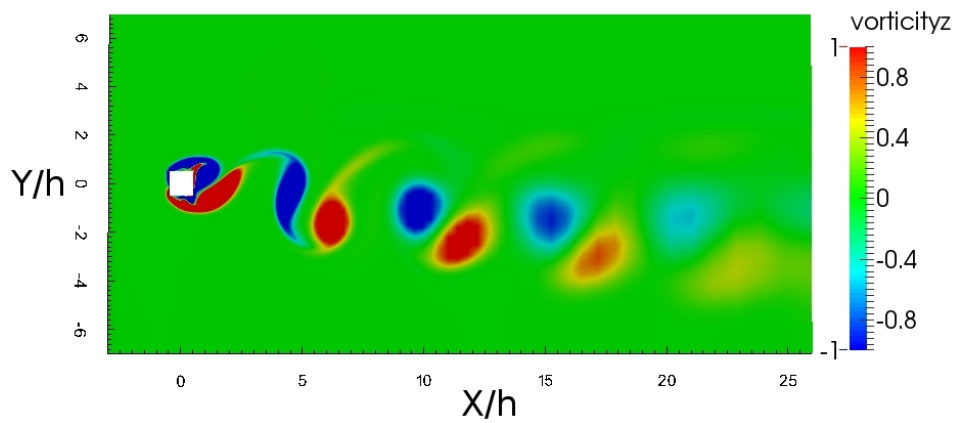
We report a new mode of antisymmetric vortex shedding where alternate structures of vortex dipoles arrange themselves in a zig-zag pattern and is represented by the symbol (\triangleleft) in figure 2.5. Vorticity plot for $f_e/f_o = 1$ and $A/h = 0.7$ is shown in figure 2.15(a). In the vicinity of the cylinder, shedding resembles an S-II mode. But further downstream, these dipoles undergo rearrangement into an antisymmetric pattern. We therefore refer to this mode as S-II-A-II to represent an S-II mode in the vicinity of the cylinder and A-II mode, an alternating pattern of dipoles, further downstream. The spectrum of the drag and lift coefficients shown in figures 2.15(b) and 2.15(c) reveals that shedding is locked onto the excitation frequency f_e .

2.3.7 Effect of varying amplitude at a fixed excitation frequency

The region of superposition and lock-on found in the present simulations are in agreement with those found by Minewitsch *et al.*[17]. Various dominant frequencies in the spectrum

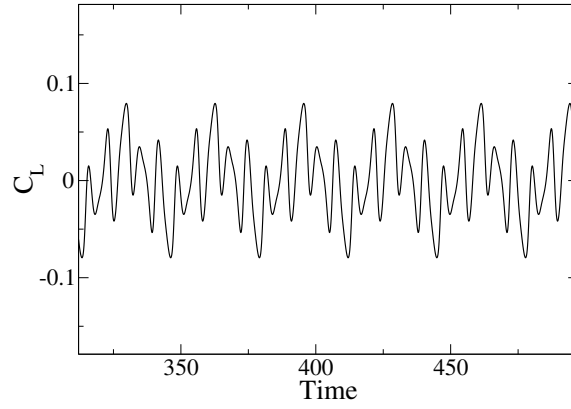


(a)

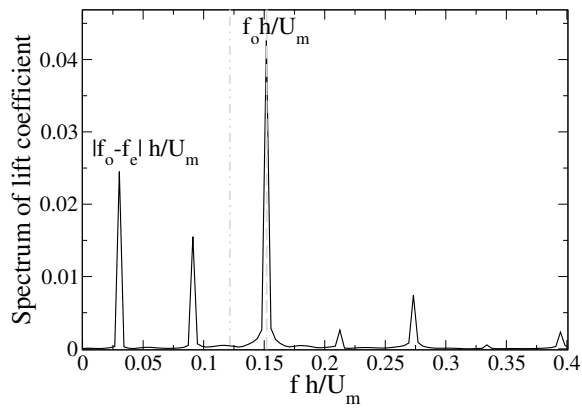


(b)

Figure 2.13: (a) Vortex flapping mode obtained at $A/h=0.4$ and $f_e/f_o=0.8$ and (b) vortex shedding at an angle but with no flapping obtained at $A/h=0.4$ and $f_e/f_o=1$. In both cases, the cylinder center is at a distance of $8h$ from inlet.

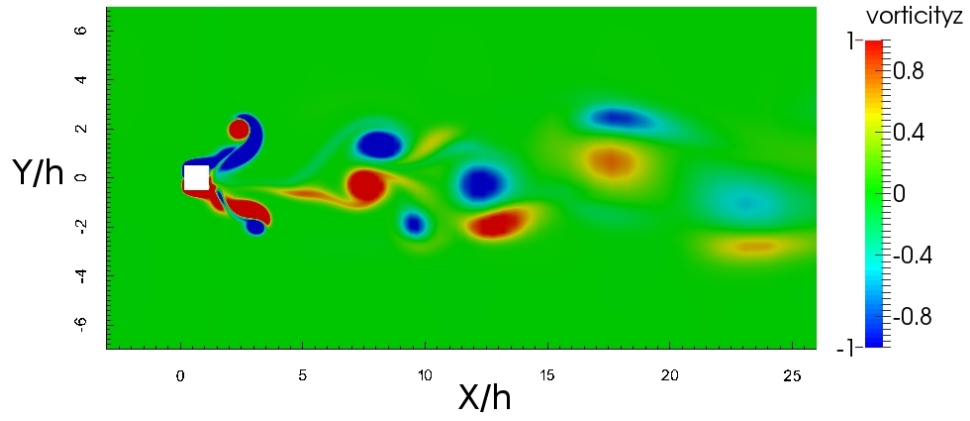


(a)

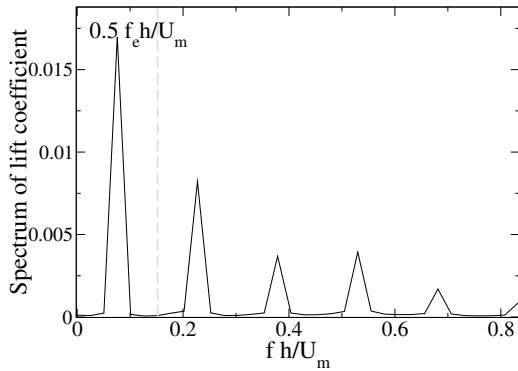


(b)

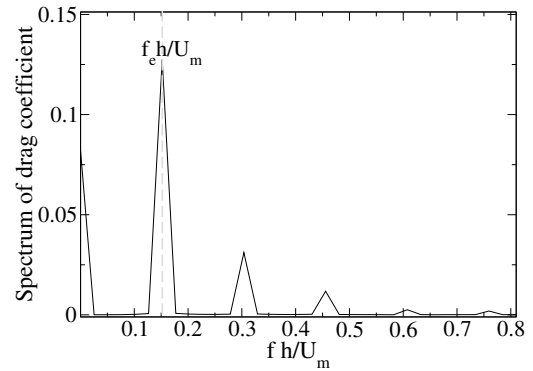
Figure 2.14: (a) Variation of lift coefficient with time and (b) spectrum of lift coefficient for $A/h = 0.4$ and $f_e/f_o=0.8$ corresponding to the flapping mode of shedding.



(a)



(b)



(c)

Figure 2.15: (a) Vorticity contours for the S-II-A-II mode at $f_e/f_o = 1$ and $A/h = 0.7$ showing an S-II like shedding in the vicinity of the cylinder and an anti-symmetric arrangement of the dipoles further downstream, (b) spectrum of lift coefficient and (c) spectrum of drag coefficient. In Figure 2.15(a), the cylinder center is at a distance of $8h$ from inlet.

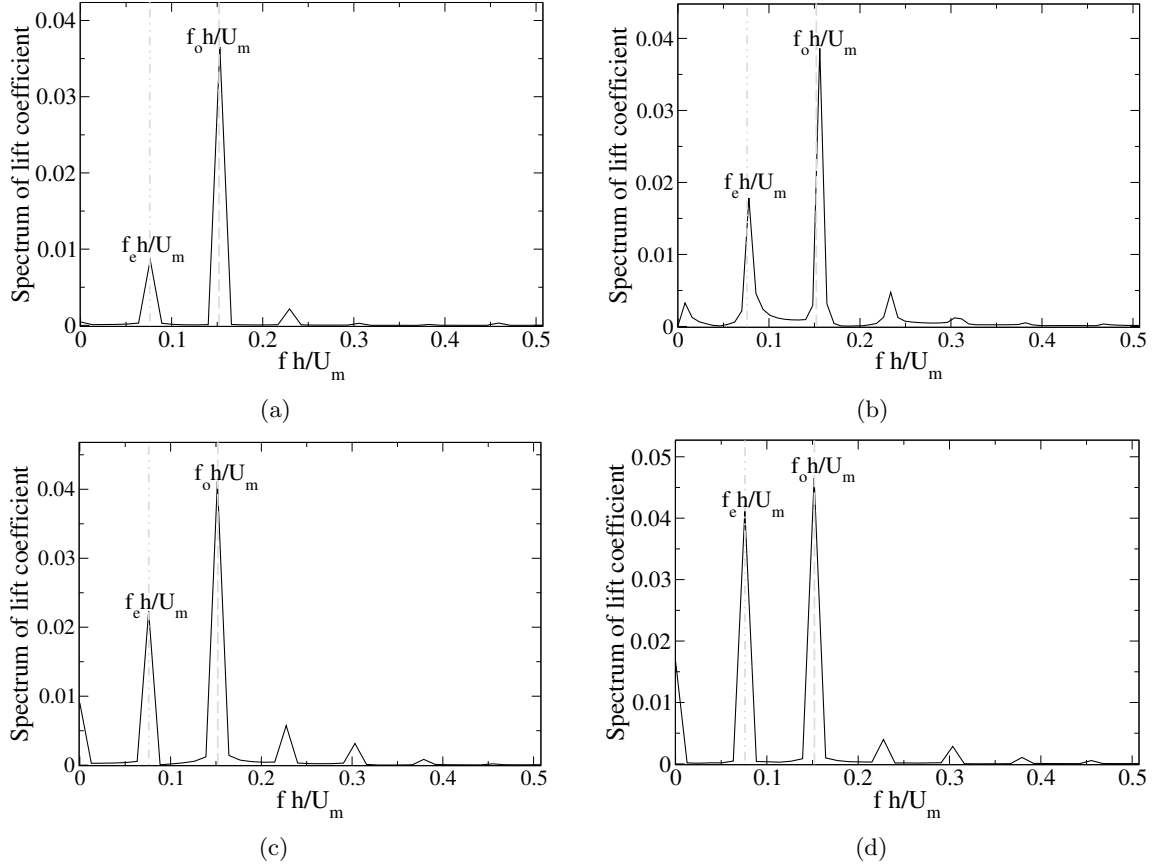


Figure 2.16: Plot of spectrum of lift coefficient obtained at a fixed frequency ratio of $f_e/f_o = 0.5$ and varying the amplitude ratio: (a) $A/h = 0.1$, (b) $A/h = 0.3$, (c) $A/h = 0.5$ and (d) $A/h = 0.7$.

of lift coefficient reported by Minewitsch *et al.*[17] by varying amplitude ratio, A/h , at different frequency ratio's, f_e/f_o , are also found in the present simulations. We decipher the role of amplitude of excitation on the frequency spectrum, we present results for three different frequency ratios, $f_e/f_o = 0.5$, $f_e/f_o = 2.5$ and $f_e/f_o = 4$. These frequency ratios cover a wide area in the parametric space of figure 2.5.

We first present the results for $f_e/f_o = 0.5$. Figure 2.16 shows frequency spectrum of lift coefficient at four different amplitude ratios, $A/h = 0.1, 0.3, 0.5, 0.7$. For this frequency ratio, the ratio of the maximum body velocity to the inlet velocity increases from 0.0477 to 0.334 as amplitude ratio increases from 0.1 to 0.7. It can be seen from the frequency spectrum of lift coefficient that as the amplitude ratio increases, the strength of the peak at f_e progressively increases and eventually becomes comparable to the peak at f_o , the frequency

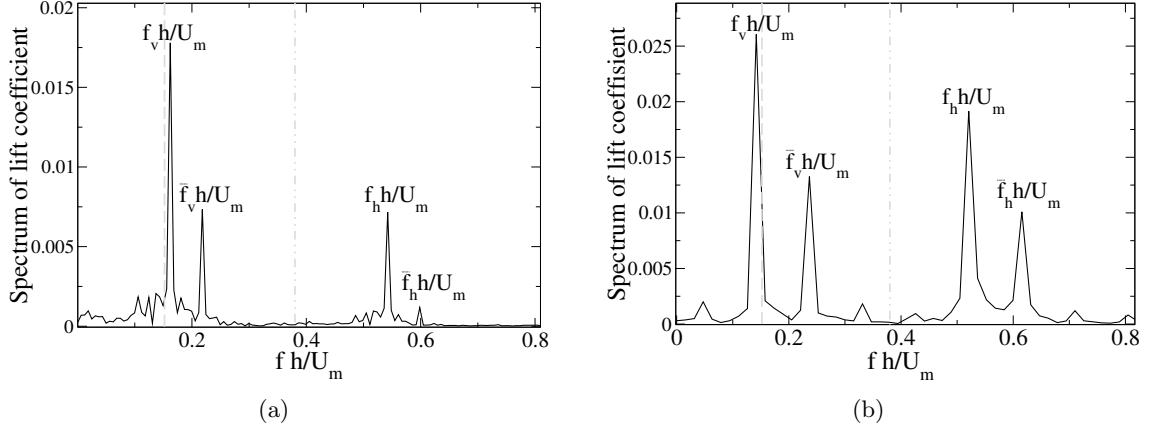


Figure 2.17: Plot of spectrum of lift coefficient obtained at (a) $A/h=0.3$ and $f_e/f_0=2.5$ and (b) $A/h=0.4$ and $f_e/f_0=2.5$.

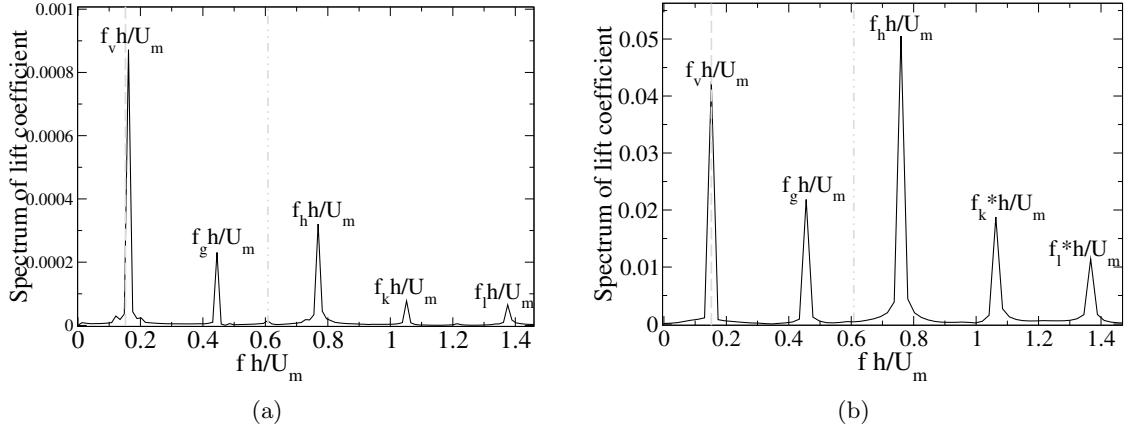


Figure 2.18: Plot of spectrum of lift coefficient obtained at (a) $A/h=0.2$ and $f_e/f_0=4$ and (b) $A/h=0.3$ and $f_e/f_0=4$.

of vortex shedding for a stationary cylinder, suggesting an eventual competition between natural frequency, f_o , of the unperturbed system and the external excitation frequency, f_e . It is therefore not surprising that the system become chaotic on further increase in amplitude of oscillation as is commonly expected in most nonlinear oscillators when forced with an external excitation. The smaller peaks in the frequency spectrum are higher harmonics corresponding to $(f_o + f_e)$, $(f_o + 2f_e)$ and so on.

In the case of $f_e/f_0 = 2.5$, figure 2.17(a) shows the spectrum of lift coefficient for two different amplitude ratios, $A/h = 0.3$ and 0.4 . Because of the higher forcing frequency, more frequencies emerge in the system. The dominant frequencies are $f_v (\approx f_o)$, $f_h = |f_e + f_v|$,

\bar{f}_v ($\approx f_e/2$) and \bar{f}_h ($= \bar{f}_v + f_e$). Note that this frequency ratio is just beyond to the window of lock on shown in figure 2.3. If the system were to be in a lock-on regime, then we expect f_v to be identically equal to $f_e/2$. We therefore see remnants of the lock-on frequency represented by \bar{f}_v and \bar{f}_h . This result is similar to that obtained by Minewitsch *et al.*[17] for $f_e/f_o=2.4$ and $A/h = 0.35$. As the amplitude ratio is increased to 0.4 there is significant increase in the influence of f_h and \bar{f}_h and a minor increase in the influence of \bar{f}_v as can be seen in figure 2.17(b). A further increase in excitation frequency to $f_e/f_o = 4$ at $A/h = 0.2$ reveals an abundance of combination frequencies such as $f_g = |f_e - f_o|$, $f_h = |f_e + f_o|$, $f_k = |2f_e - f_o|$ and $f_l = |2f_e + f_o|$ as shown in figure 2.18(a). A minor increase in amplitude ratio to 0.3 propels the dominance of f_h and other harmonics (figure 2.18(b)). Similar results have been found for $f_e/f_o=3, 4.5$ and 5. In summary, an increase in amplitude promotes greater competition between the modes and eventually leads to chaotic regimes as shown in figure 2.5.

2.3.8 Chaotic modes

Several chaotic modes have been observed in our simulations and are represented by the symbol (\square) in figure 2.5. Each of these chaotic modes occur in different regions of the parametric space and therefore possess different characteristics. We discuss just three representative cases in figure 2.19, one, in the large amplitude and small frequency range, two, in the small amplitude and large frequency range, and three, in a moderate amplitude and frequency range.

Figure 2.19(a) shows the phase portrait with the lift coefficient plotted against the drag coefficient for $A/h = 1.125$ and $f_e/f_o = 1.026$. A complex two lobed non-repetitive structure is seen and is indicative of a chaotic flow. The frequency spectrum of the lift coefficient shown in figure 2.19(b) shows a broadband spectrum but with a dominant peak near f_e or f_o shown by the dashed/dashed-dot vertical lines. Since this chaotic mode occurs in the vicinity of S-II-I mode reported earlier (see figures 2.5 and 2.6), remnants of the dominant frequency of the S-II-I at frequency f_e is visible. Figure 2.19(c) shows the

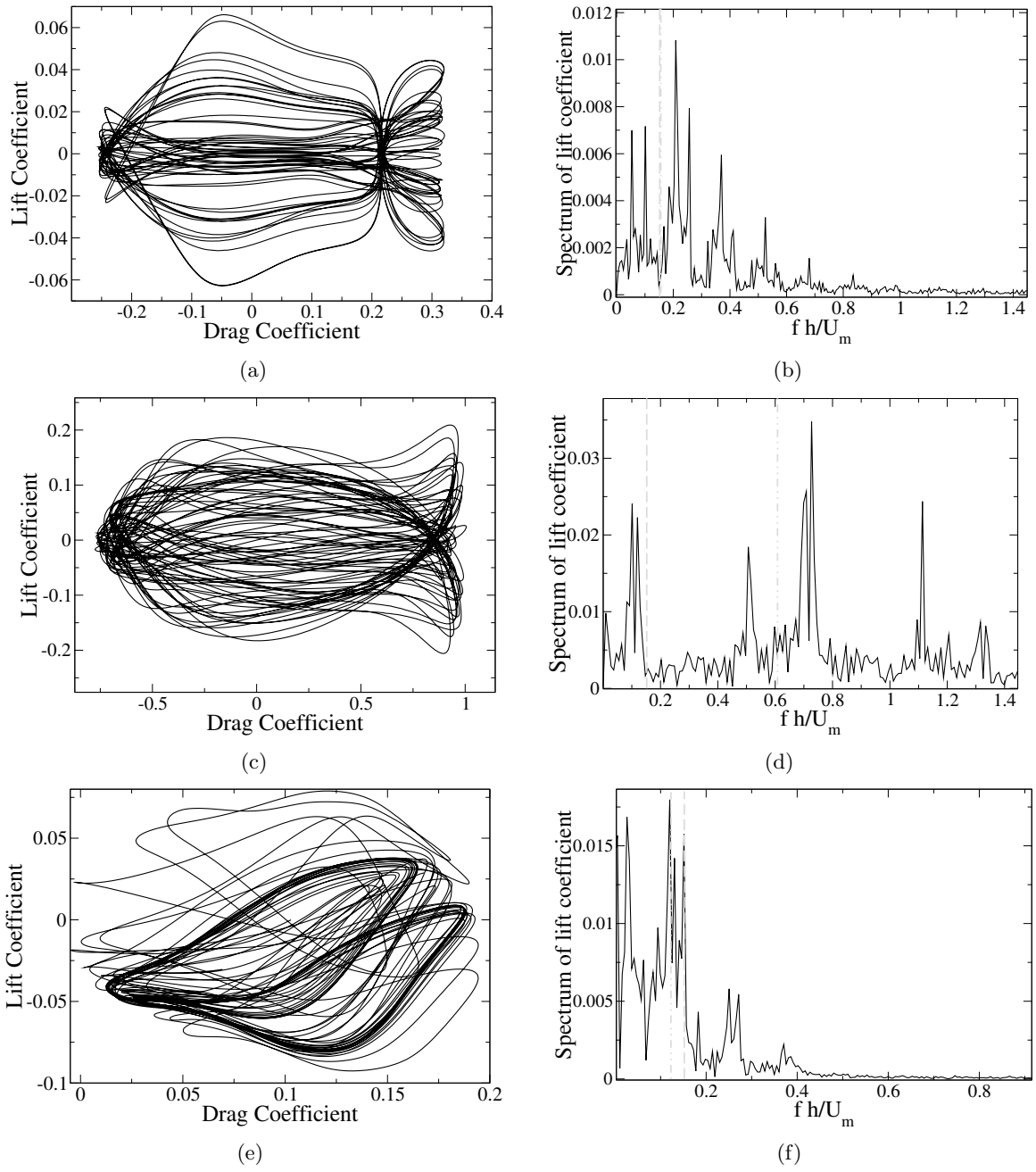


Figure 2.19: Phase plot of lift vs drag coefficient (left panels) and frequency spectrum of lift coefficient (right panels) obtained at: (a)-(b) $A/h = 1.125$ and $f_e/f_o = 1.026$, (c)-(d) $A/h = 0.4$ and $f_e/f_o = 4$ & (e)-(f) $A/h = 0.6$ and $f_e/f_o = 0.807$.

phase portrait for $A/h = 0.4$ and $f_e/f_o = 4$. This chaotic mode occurs in the vicinity of the S-IV-D modes discussed earlier. Therefore the first dominant peak is closer to f_e (figure 2.19(d)) and a subdominant peak occurs closer to f_o . The above two modes share one characteristic feature: they become chaotic when the strength of the forcing, determined by either a large amplitude or large frequency, becomes comparable to the strength of the inlet flow. Therefore these chaotic modes occur near the solid curved line in figure 2.5.

Chaos can also occur through a mode competition feature during the transition from antisymmetric to symmetric modes as discussed in Srikanth *et al.*[10]. Such a competition occurs when the vortex flapping mode transitions to a S-II-I mode with increase in amplitude of forcing. Figure 2.19(e) and 2.19(f) shows the phase portrait and spectrum of lift coefficient at $A/h = 0.6$ and $f_e/f_o = 0.807$. The spectrum is dominated by the frequencies f_e and f_o as expected from modes which occur in the vicinity S-II-I mode or the flapping mode.

2.3.9 Ambiguous mode

Apart from symmetric, anti-symmetric and chaotic modes, we find modes of vortex shedding which do not lend themselves to a clear classification. We therefore refer to these modes as ‘ambiguous’ modes and are represented by symbols (\triangle) and (\triangleright) in figure 2.5.

Not surprisingly, the two types of ambiguous modes found in the present simulations occur in very different parts of the parametric space. The first ambiguous mode (Ambiguous-I) is found in the vicinity of $A/h = 0.2$ and $f_e/f_o = 4$ and its vorticity contours at a particular time is shown in figure 2.20(a) and its frequency spectrum was shown earlier in figure 2.18(a). This mode loosely resembles an S-IV mode in the near wake, but with an antisymmetric character embedded within it. The mode clearly breakdown into an antisymmetric vortex pattern further downstream.

Another ambiguous mode (Ambiguous-II) is found in the vicinity of $f_e/f_o=1.0375$ and $A/h = 0.875$. Vorticity contours for this mode, shown in figure 2.20(b), reveals a complex spatial arrangement of vortices but this mode is clearly periodic as evident from

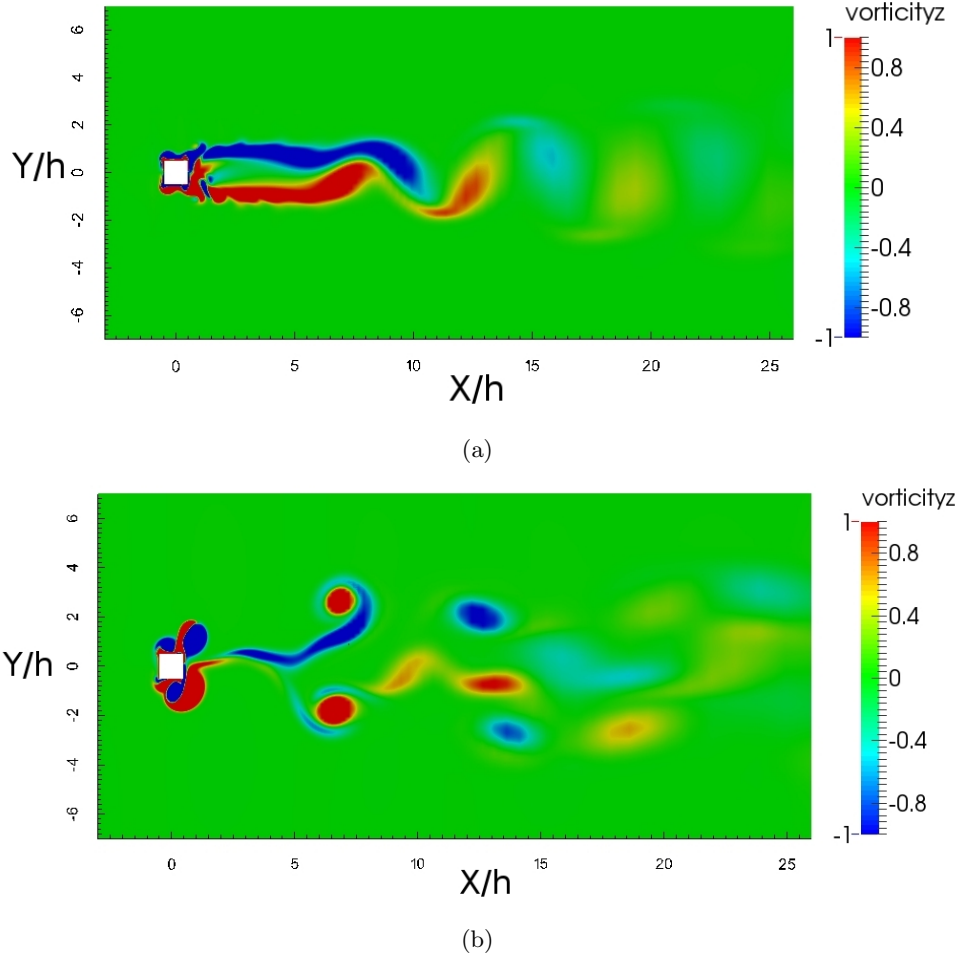


Figure 2.20: Vorticity contours of ambiguous modes obtained with (a) $A/h = 0.2$ and $f_e/f_o=4.5$, (b) $A/h=0.875$ and $f_e/f_o=1.0375$. In both cases, the cylinder center is at a distance of $8h$ from inlet.

the spectrum of lift coefficient and phase plot of lift vs drag coefficient in figure 2.21.

2.4 Conclusion

In this work, a systematic study of vortex shedding past an in-line oscillating square cylinder at a Reynolds number of 200 is presented. The amplitude of cylinder oscillation and the frequency of excitation were varied, spanning over 100 computer simulations, to reveal a number of new features. Some of these features such as the observation of two new symmetric modes, S-II-I and S-IV-D, are being reported for the first time, while other

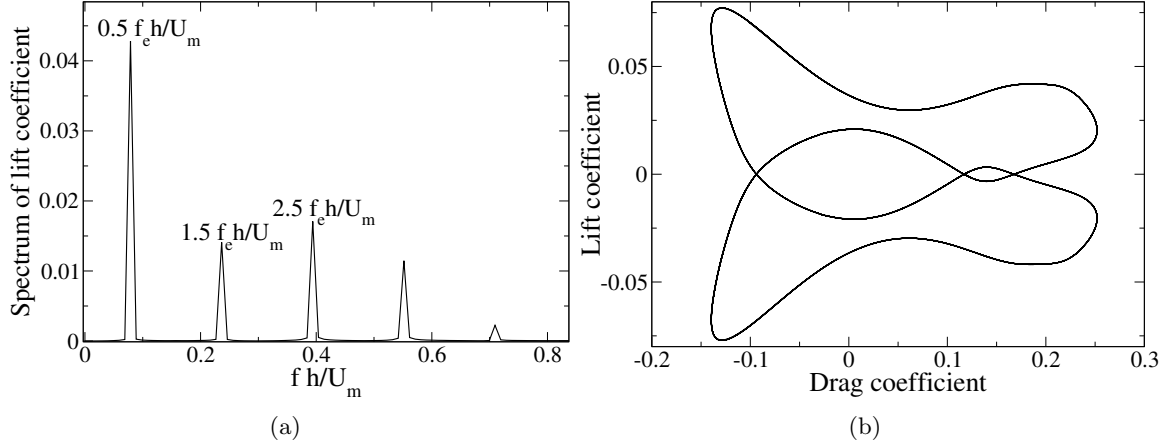


Figure 2.21: Characteristics of ambiguous-II mode of figure 2.20(b): (a) spectrum of lift coefficient, (b) phase plot of lift vs drag coefficient showing that this is a non-chaotic mode.

features such as vortex flapping modes and chaotic modes have been investigated in greater detail. A summary of all the simulations, shown in figure 2.5, shows clustering of modes based on the structure of the vortex street.

In the S-II-I mode of figure 2.6, two pairs of vortices are shed for every cycle of cylinder oscillation symmetrically, of which the secondary pair gets sheared away downstream. This results in a stable S-I mode downstream of the cylinder. This mode is found in the top-left region of the parameter space of figure 2.5 which corresponds to moderate/large values of amplitude ratio and small frequency ratio. In the bottom-right region of the parameter space of figure 2.5 which corresponds to low values of amplitude ratio but high values of frequency ratio, we find another symmetric mode which we name S-IV-D. This mode is characterised by two pairs of vortex dipoles shed on each side of the cylinder in every cycle of cylinder oscillation. A systematic study of these symmetric modes is presented in the paper. In addition, we also study the emergence of the S-IV-D mode from an antisymmetric state as a function of the frequency. We find that the length of the symmetric region increases with frequency and obeys a power-law with a negative exponent. This suggests that a true S-IV-D mode (even in a domain of infinite length) emerges when the frequency reaches a critical value.

Another interesting feature observed in the present simulations is the emergence of the

so-called ‘flapping mode’ where the entire vortex street oscillates about the centreline. This mode is characterised by two time-scales, a fast time scale at frequency f_o corresponding to the shedding of individual vortices from the cylinder and a slow time scale at frequency $|f_o - f_e|$ corresponding to the flapping frequency. As $f_e \rightarrow f_o$, the time scale of flapping which is proportional to $1/|f_e - f_o|$ becomes progressively longer and eventually leading to an oblique shedding when $f_e = f_o$. We also find a range of new combination frequencies such as $f_h = |f_v + f_e|$, $f_g = |f_e - f_o|$, $f_k = |2f_e - f_o|$ and $f_l = |2f_e + f_o|$ appear with increase in either amplitude or frequency of excitation. Interactions between these new frequencies often leads to chaos. We find that such chaos usually occurs when the cylinder velocity ($A \times 2\pi f_e$) becomes comparable to the inlet velocity, U_m , as shown by the solid curved line in figure 2.5. Another route to chaos observed in our analysis is a mode-competition mechanism during the transition from an antisymmetric shedding to a symmetric shedding.

A number of issues remain unexplored and are briefly discussed below. Some of these questions are currently being addressed and will be presented elsewhere. A systematic bifurcation diagram for the transition to chaos when shedding transforms from antisymmetric to symmetric type is unknown. The evolution of the different modes obtained in this paper by varying the two parameters (amplitude ratio and frequency ratio) is currently being studied with the help of linear stability analysis. It is well known that the antisymmetric pattern found in the classical von Kármán vortex street can be predicted using a local stability analysis on a stationary wake profile (see Hultgren and Agarwal[21]). We are attempting a similar analysis on an oscillating velocity profile.

Chapter 3

Linear Stability Analysis

3.1 Analysis

3.1.1 Formulation

We first begin by considering oscillating base velocity profile as follows:

$$U(y, t) = 1 - U_0 e^{-y^2/\delta^2} + U_1 e^{-y^2/\delta^2} \sin(\omega t) \quad (3.1)$$

where U_0 is the amplitude of the steady component and U_1 is the amplitude of the oscillating component. Here $\omega=2\pi f_e$, $\delta=0.1$, $U_1=\alpha\delta\omega$ and $-2<y<2$. The use of δ is done to reduce the domain in y-direction and achieve convergence with less number of modes.

The 2-D Euler and Inviscid Equation is as follows:

Continuity Equation:

$$\frac{\partial \tilde{u}}{\partial x} + \frac{\partial \tilde{v}}{\partial y} = 0 \quad (3.2)$$

Momentum Equation:

$$\frac{\partial \tilde{u}}{\partial t} + \tilde{u} \frac{\partial \tilde{u}}{\partial x} + \tilde{v} \frac{\partial \tilde{u}}{\partial y} = -\frac{1}{\rho} \frac{\partial \tilde{p}}{\partial x} \quad (3.3)$$

$$\frac{\partial \tilde{v}}{\partial t} + \tilde{v} \frac{\partial \tilde{v}}{\partial x} + \tilde{v} \frac{\partial \tilde{v}}{\partial y} = -\frac{1}{\rho} \frac{\partial \tilde{p}}{\partial y} \quad (3.4)$$

where \tilde{u} , \tilde{v} and \tilde{p} are total quantities.

Now, we perturb the system linearly as follows:

$$\tilde{u} = U(y, t) + u(x, y, t) \quad (3.5)$$

$$\tilde{v} = v(x, y, t) \quad (3.6)$$

$$\tilde{p} = P(x, y, t) + p(x, y, t) \quad (3.7)$$

here $u, v \ll U$ and $p \ll P$

Assuming normal modes, the streamfunction of a small perturbation to the base flow can be written in the form:

$$\psi(x, y, t) = \phi(y, t)e^{i\alpha x}, \quad (3.8)$$

where α is dimensionless wave number of the disturbance,

On eliminating pressure from the two momentum equation, we obtain the time dependent Rayleigh equation:

$$L\left(\frac{\partial \phi}{\partial t}\right) = \left\{i\alpha \left[\frac{\partial^2 U}{\partial y^2} - UL\right]\right\}\phi \quad (3.9)$$

where $L = \frac{\partial^2}{\partial y^2} - \alpha^2$. The boundary condition is given by disturbance velocity vanishing at the boundaries and hence

$$\phi = \frac{\partial \phi}{\partial y} = 0 \quad \text{at} \quad y = \pm 2 \quad (3.10)$$

The approach is to expand $\phi(y, t)$ in complete set of functions of y which satisfy the boundary

conditions.

3.1.2 Expansion Functions

We have used the following functions as the expansion functions as they are orthogonal and satisfy the boundary conditions:

$$\phi_n(y) = \sin\left(\frac{n\pi(y+L)}{2L}\right) \quad \text{where } -2 < y < 2 \quad (3.11)$$

3.1.3 Galerkin Equation

We assume $\phi(y, t) = \sum_1^n a_n(t)\phi_n(y)$. Then according to Galerkin Method, error is made orthogonal to each ϕ_n to get optimal approximation. So, the following system of ODEs for the amplitude coefficients are obtained:

$$\hat{\mathbf{Q}} \frac{d\mathbf{a}}{dt} = i\alpha \hat{\mathbf{V}}(t)\mathbf{a}, \quad (3.12)$$

where

$$\hat{Q}_{mn} = \langle L\phi_n, \phi_m \rangle,$$

$$\hat{V}_{mn}(t) = \langle U_{yy}\phi_n - UL\phi_n \rangle, \phi_m \rangle,$$

$$\langle a, b \rangle \equiv \int_{-2}^2 ab \, dy.$$

The matrix $\hat{\mathbf{Q}}$ is constant and symmetric. On inverting matrix $\hat{\mathbf{Q}}$ we get:

$$\frac{d\mathbf{a}}{dt} = i\alpha \mathbf{V}(t)\mathbf{a} \quad (3.13)$$

Defining $\mathbf{A}(t) = i\alpha \mathbf{V}(t)$, we get

$$\frac{d\mathbf{a}}{dt} = \mathbf{A}(t)\mathbf{a}, \quad (3.14)$$

where $\mathbf{A}(t)$ is periodic in time.

3.1.4 Floquet Theorem

Let $\mathbf{F}(t)$ be the fundamental matrix of N-dimensional time-dependent Galerkin equation.

Then by the use of Floquet theorem, $\mathbf{F}(t)$ can be represented as:

$$\mathbf{F}(t) = \mathbf{B}(t)e^{t\mathbf{C}},$$

where \mathbf{B} is a 2π -periodic matrix in t with period $\frac{2\pi}{\omega}$, \mathbf{C} is a constant matrix and the initial value of \mathbf{F} can be taken to be identity matrix:

$$\mathbf{F}(0) = \mathbf{I}.$$

Since $\mathbf{B}(t) = \mathbf{B}(t + \frac{2\pi}{\omega})$, it follows that

$$\mathbf{F}(2\pi) = e^{\frac{2\pi}{\omega}\mathbf{C}}.$$

The eigenvalues λ (called Floquet exponents) of \mathbf{C} are obtained from the eigenvalues μ of $\mathbf{F}(\frac{2\pi}{\omega})$ by

$$\lambda = \frac{2\pi}{\omega} \ln(\mu)$$

Let λ_1 be the Floquet exponent with the largest real part. If $\text{Re}(\lambda_1) \neq 0$, then the flow is unstable or stable to infinitesimal disturbances according as $\text{Re}(\lambda_1) > 0$ or $\text{Re}(\lambda_1) < 0$ respectively. If $\text{Re}(\lambda_1) = 0$, and if λ_1 has multiplicity greater than one, then the flow is unstable. The actual values of λ will be $\delta X \lambda$ due to the use of δ in the base velocity profile. But these values of λ are sufficient to derive results.

The eigenvector $a^{(1)}(\frac{2\pi}{\omega})$, which is the associated eigenvector of λ_1 can then be calculated and used to find the stream function $\psi(2\pi)$.

The eigenvector $a^{(1)}$ can then be calculated by integrating (3.14) starting with the initial condition:

$$\mathbf{a}^{(1)}(0) = e^{-2\pi\lambda_1} \mathbf{a}^{(1)}(\frac{2\pi}{\omega}),$$

Thus by calculating the amplitude coefficients, we can calculate the stream function ψ , thereby calculating the perturbation velocities and finally perturbation vorticity. On superimposing the vorticity of base state and perturbation vorticity we can get the dominant shedding mode.

3.2 Results

We obtained two different kinds of modes for the parametric study that we conducted, namely, the symmetric mode and the anti-symmetric mode. The symmetric mode is shown in figure 3.1 for $\alpha=1$ and $f_e=1$. Here, 3.1(a) represents contours of perturbed vorticity and 3.1(b) represents superposition of mean and perturbed vorticity. This mode is found to occur in regions of low α .

The antisymmetric mode is shown in figure 3.2 for $\alpha=10$ and $f_e=1$. Here, 3.2(a) represents contours of perturbed vorticity and 3.2(b) represents superposition of mean and perturbed vorticity. This mode is similar to the karman vortex street found behind a flow past stationary cylinder.

Figure 3.3 shows the nature of modes obtained at different values of f_e and α . Here, 1 stands for symmetric mode and 0 stands for antisymmetric mode. The results for $\alpha > 18$ cannot be trusted as the λ value is very close to zero for this region.

Figure 3.4 shows the variation of λ for different values of f_e and α from different views. In these plots, same color represents same value of f_e .

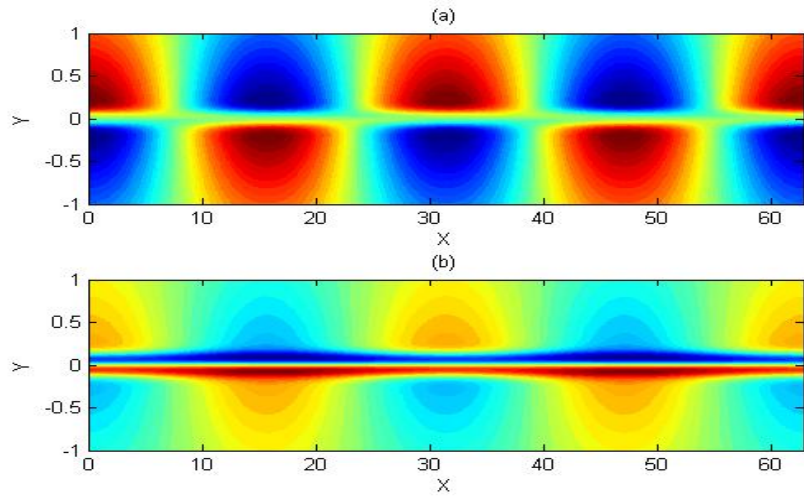


Figure 3.1: Plots showing symmetric mode obtained for $\alpha=0.2$ and $f_e=1$. (a) represents contours of perturbed vorticity and (b) represents superposition of mean and perturbed vorticity.

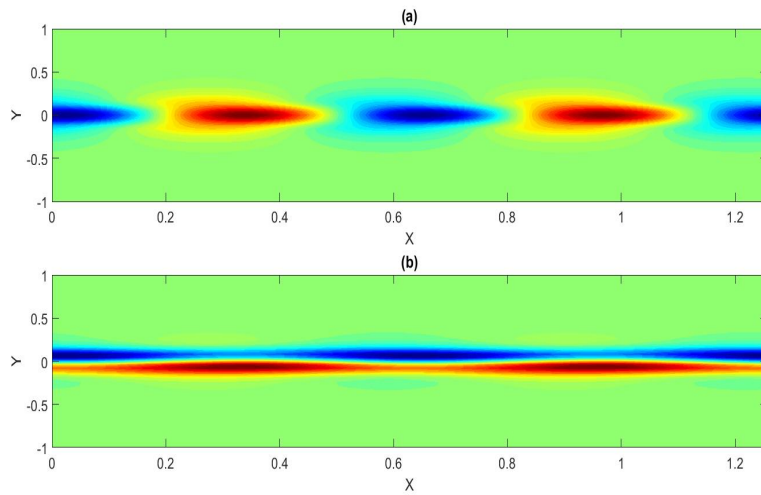


Figure 3.2: Plots showing the antisymmetric modes obtained for $\alpha=10$ and $f_e=1$. (a) represents contours of perturbed vorticity and (b) represents superposition of mean and perturbed vorticity.

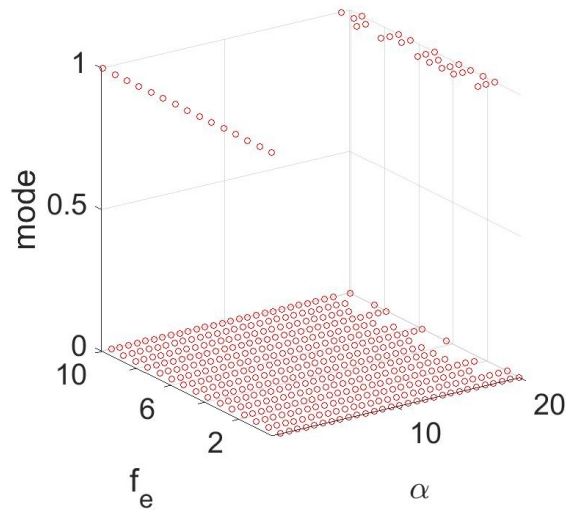


Figure 3.3: Plot showing the nature of modes obtained at different values of f_e and α . 1 stands for symmetric modes and 0 stands for antisymmetric modes. The results for $\alpha_i 18$ cannot be trusted as the λ value is very close to zero for this region.

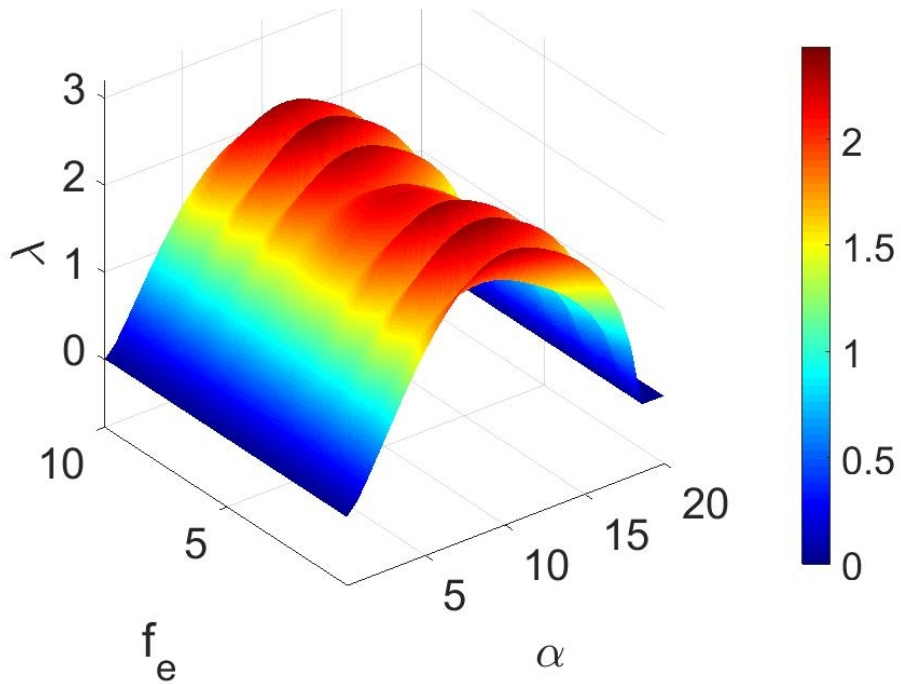


Figure 3.4: Plot showing the variation of λ for different values of f_e and α . Same color represents same value of f_e

3.3 Conclusion

The linear stability analysis shows the presence of two different modes, namely the symmetric and anti-symmetric mode. The symmetric mode is found to occur only for lower values of α . This indicates that a high amplitude of the oscillating component is necessary to actuate this mode which is consistent with the findings of DNS results which shows presence of symmetric modes at high amplitudes and low frequencies.

Chapter 4

Future Outlook

The use of oscillating inlet boundary condition for study of inline oscillations of bluff bodies have always created problems as the researchers have not been able to fully explore the parametric plane. The DNS studies conducted with the use of dynamic meshing can be used to explore bluff body dynamics like that of rectangular cylinder, thin plates, etc beyond the regions that were not explored previously.

The linear stability code can be used for study of pulsating flows like flow between thin plates, flow in a channel, blood flow, etc.

Chapter 5

Appendix-1

The following is the blockMeshDict file

```
/*-----* C++ *-----*\
| ===== |
| \\      / F i e l d      | OpenFOAM: The Open Source CFD Toolbox |
| \\      / O p e r a t i o n      | Version: 2.3.0 |
|  \\    / A n d      | Web: www.OpenFOAM.org |
|  \\\\   M a n i p u l a t i o n   | |
\*-----*/

FoamFile
{
    version      2.0;
    format       ascii;
    class        dictionary;
    object       blockMeshDict;
}

// * * * * * //

//changeom(//)changequote([,])

// Define all the constants
```


(4 2.5 0)	//28
(26 2.5 0)	//29
(-8 9 0)	//30
(-1 9 0)	//31
(-0.5 9 0)	//32
(0.5 9 0)	//33
(4 9 0)	//34
(26 9 0)	//35
(-8 -9 0.05)	//36
(-1 -9 0.05)	//37
(-0.5 -9 0.05)	//38
(0.5 -9 0.05)	//39
(4 -9 0.05)	//40
(26 -9 0.05)	//41
(-8 -2.5 0.05)	//42
(-1 -2.5 0.05)	//43
(-0.5 -2.5 0.05)	//44
(0.5 -2.5 0.05)	//45
(4 -2.5 0.05)	//46
(26 -2.5 0.05)	//47
(-8 -0.5 0.05)	//48
(-1 -0.5 0.05)	//49
(-0.5 -0.5 0.05)	//50
(0.5 -0.5 0.05)	//51
(4 -0.5 0.05)	//52
(26 -0.5 0.05)	//53
(-8 0.5 0.05)	//54
(-1 0.5 0.05)	//55
(-0.5 0.5 0.05)	//56
(0.5 0.5 0.05)	//57
(4 0.5 0.05)	//58
(26 0.5 0.05)	//59
(-8 2.5 0.05)	//60
(-1 2.5 0.05)	//61
(-0.5 2.5 0.05)	//62
(0.5 2.5 0.05)	//63

```

(4 2.5 0.05) //64
(26 2.5 0.05) //65
(-8 9 0.05) //66
(-1 9 0.05) //67
(-0.5 9 0.05) //68
(0.5 9 0.05) //69
(4 9 0.05) //70
(26 9 0.05) //71

);

blocks
(
  hex (0 1 7 6 36 37 43 42) (34 35 1) simpleGrading (0.025 0.025 1)
//0
  hex (1 2 8 7 37 38 44 43) (30 35 1) simpleGrading (1 0.025 1)
//1
  hex (2 3 9 8 38 39 45 44) (60 35 1) simpleGrading (1 0.025 1)
//2
  hex (3 4 10 9 39 40 46 45) (210 35 1) simpleGrading (1 0.025 1)
//3
  hex (4 5 11 10 40 41 47 46) (75 35 1) simpleGrading (40 0.025 1)
//4
  hex (6 7 13 12 42 43 49 48) (34 120 1) simpleGrading (0.025 1 1)
//5
  hex (7 8 14 13 43 44 50 49) (30 120 1) simpleGrading (1 1 1) //6
  hex (8 9 15 14 44 45 51 50) (60 120 1) simpleGrading (1 1 1) //7
  hex (9 10 16 15 45 46 52 51) (210 120 1) simpleGrading (1 1 1) //8
  hex (10 11 17 16 46 47 53 52) (75 120 1) simpleGrading (40 1 1) //9
  hex (12 13 19 18 48 49 55 54) (34 60 1) simpleGrading (0.025 1 1)
//10
  hex (13 14 20 19 49 50 56 55) (30 60 1) simpleGrading (1 1 1) //11
  hex (15 16 22 21 51 52 58 57) (210 60 1) simpleGrading (1 1 1) //12
  hex (16 17 23 22 52 53 59 58) (75 60 1) simpleGrading (40 1 1) //13

```

```

    hex (18 19 25 24 54 55 61 60) (34 120 1) simpleGrading (0.025 1 1)
//14
    hex (19 20 26 25 55 56 62 61) (30 120 1) simpleGrading (1 1 1) //15
    hex (20 21 27 26 56 57 63 62) (60 120 1) simpleGrading (1 1 1) //16
    hex (21 22 28 27 57 58 64 63) (210 120 1) simpleGrading (1 1 1) //17
    hex (22 23 29 28 58 59 65 64) (75 120 1) simpleGrading (40 1 1) //18
    hex (24 25 31 30 60 61 67 66) (34 35 1) simpleGrading (0.025 40 1)
//19
    hex (25 26 32 31 61 62 68 67) (30 35 1) simpleGrading (1 40 1) //20
    hex (26 27 33 32 62 63 69 68) (60 35 1) simpleGrading (1 40 1)
//21
    hex (27 28 34 33 63 64 70 69) (210 35 1) simpleGrading (1 40 1) //22
    hex (28 29 35 34 64 65 71 70) (75 35 1) simpleGrading (40 40 1)
//23
);

```

boundary

```

(
    top
    {
        type symmetryPlane;
        faces
        (
            (30 31 67 66)
            (31 32 68 67)
            (32 33 69 68)
            (33 34 70 69)
            (34 35 71 70)
        );
    }
    inlet
    {
        type patch;
        faces

```

```

    (
      (30 66 60 24)
      (24 60 54 18)
      (18 54 48 12)
      (12 48 42 6)
      (6 42 36 0)
    );
  }
  bottom
  {
    type symmetryPlane;
    faces
    (
      (0 36 37 1)
      (1 37 38 2)
      (2 38 39 3)
      (3 39 40 4)
      (4 40 41 5)
    );
  }
  outlet
  {
    type patch;
    faces
    (
      (35 29 65 71)
      (29 23 59 65)
      (23 17 53 59)
      (17 11 47 53)
      (11 5 41 47)
    );
  }
  cylinder
  {
    type wall;
    faces

```

```

(
    (20 56 50 14)
    (14 50 51 15)
    (21 15 51 57)
    (56 20 21 57)

);
}
front
{
    type empty;
    faces
(
(0 1 7 6)
(1 2 8 7)
(2 3 9 8)
(3 4 10 9)
(4 5 11 10)
(6 7 13 12)
(7 8 14 13)
(8 9 15 14)
(9 10 16 15)
(10 11 17 16)
(12 13 19 18)
(13 14 20 19)
(15 16 22 21)
(16 17 23 22)
(18 19 25 24)
(19 20 26 25)
(20 21 27 26)
(21 22 28 27)
(22 23 29 28)
(24 25 31 30)
(25 26 32 31)
(26 27 33 32)
(27 28 34 33)

```

```
(28 29 35 34)
);
}
back
{
    type empty;
    faces
    (
        (37 36 42 43)
        (37 43 44 38)
        (39 38 44 45)
        (40 39 45 46)
        (41 40 46 47)
        (43 42 48 49)
        (44 43 49 50)
        (45 44 50 51)
        (46 45 51 52)
        (47 46 52 53)
        (49 48 54 55)
        (50 49 55 56)
        (52 51 57 58)
        (53 52 58 59)
        (55 54 60 61)
        (56 55 61 62)
        (57 56 62 63)
        (58 57 63 64)
        (59 58 64 65)
        (61 60 66 67)
        (62 61 67 68)
        (63 62 68 69)
        (64 63 69 70)
        (65 64 70 71)
    );
}
);
```



```
mergePatchPairs
```

```
(  
);
```

```
// ***** //  
// ***** //
```

Chapter 6

Appendix-2

The following is the dynamicMeshDict file

```
/*-----* C++ *-----*\
| ===== |
| \\ / F i e l d | OpenFOAM: The Open Source CFD Toolbox |
| \\ / O p e r a t i o n | Version: 2.0.0 |
| \\ / A n d | Web: www.OpenFOAM.org |
| \\ / M a n i p u l a t i o n | |
\*-----*/

FoamFile
{
    version      2.0;
    format       ascii;
    class        dictionary;
    object       motionProperties;
}

// * * * * *

dynamicFvMesh      dynamicMotionSolverFvMesh;

twoDMotion yes; //optional

motionSolverLibs (" libfvMotionSolvers.so");
```

```
solver displacementLaplacian;
displacementLaplacianCoeffs
{
// diffusivity uniform;
// diffusivity directional (1 200 0);
// diffusivity motionDirectional (1 1000 0);
// diffusivity file motionDiffusivity;
diffusivity quadratic inverseDistance 1(cylinder);
}
```

```
//***** //
```

Chapter 7

Appendix-3

The 0-1 test for chaos

We took the time series of Lift Coefficient ($L(t)$) and concluded the occurrence of chaos by using the 0-1 test of chaos. This test was introduced by Gottwald and Melbourne (2004) [19] and its detailed implementation was given in Gottwald and Melbourne (2009) [20]. The entire code of this test and its implementation for logistic map with results can be found in Appendix 3 which can be verified with the results in Gottwald and Melbourne (2009) [20]. The main benefits of this test is that it does not require phase space reconstruction and gives binary result i.e 0 or 1 where 1 stands for chaos. The time sampling needs to be done by ensuring that the acquired value at each instant provides little information about future values at stable operation. The minimum of the average mutual information curve provides with the optimum sampling time (τ_{opt}). To get the average mutual information curve we have used the code by Eric Weeks on his website.

From the time series data $L(t)$ and $t_{i+1}-t_i=\tau_{opt}$, translation variables are obtained as follows:

$$q_c(n) = \sum_{t=1}^n p(t) \cos(tc), \quad (7.1)$$

$$r_c(n) = \sum_{t=1}^n p(t) \sin(tc) \quad (7.2)$$

where $c \in (\pi/5, 4\pi/5)$. The mean square displacement of these translation variables can be computed for different values of c as follows:

$$M_c(n) = \lim_{N \rightarrow \infty} \frac{1}{N} \sum_{t=1}^N \left(\left[q_c(t+n) - q_c(t) \right]^2 + \left[r_c(t+n) - r_c(t) \right]^2 \right) \quad (7.3)$$

where $n \ll N$. It is made sure that $n \leq n_{cut}$ where $n_{cut} = N/10$ yields good results.

The mean square displacement is indicative of the diffusive nature of the translation variables. If the dynamics is regular, then the mean square displacement is a bounded function in time and for chaotic dynamics, it scales linearly with time.

A modified mean square displacement D_c can be defined to ensure better convergence properties but with same asymptotic growth rate as

$$D_c(n) = M_c(n) - V_{osc}(n) \quad (7.4)$$

where

$$V_{osc}(c, n) = \langle p(t) \rangle^2 \left[\frac{1 - \cos nc}{1 - \cos c} \right] \quad (7.5)$$

and

$$\langle p(t) \rangle = \lim_{N \rightarrow \infty} \frac{1}{N} \sum_{t=1}^N p(t) \quad (7.6)$$

Hence by defining vectors $\xi = (1, 2, \dots, n_{cut})$ and $\delta = (D_c(1), D_c(2), \dots, D_c(n_{cut}))$, the correlation K_c given by

$$K_c = corr(\xi, \delta) \quad (7.7)$$

essentially allows one to distinguish between the two types of behaviour possible in such

systems.

To ensure robustness of the measure to outliers and spurious resonances, the median value of K_c (say K) may be taken which is obtained for different random values of c . This value of K would lie close to 1 for chaotic signals and close to 0 for regular dynamics.

The following is the code for 0-1 test along with results for logistic map.

```
clear all
close all
clc

load liftcoeff_data.txt

% x = lorenz_data(1:end,1);

x(1)=0.2;
for i=2:5500
x(i)=3.9*x(i-1)*(1-x(i-1));
end
x=x';
%% Applying the 0-1 test
% We choose phi = x1 + x2, c = 1.7;

% phi = x(1);
% c = 1.7;
% N = length(x);
%
% theta(1,1) = 0;
% for count = 2:N
%     time = t(count);
%     theta(count,1) = c*t(count) + trapz(t(1:count,1), phi*ones(count,1));
%     p(count,1) = trapz(t(1:count,1), phi.*cos(theta(1:count,1)));
% end
%
% Tmax = t(10000)
```

```

%
% M(1)=0;
% for count = 2:8000
%
%     M(count,1)= 1/t(8000)*trapz(t(1:8000),(p(count:count+8000-1)-p(1:8000)).^2);
% end

%% Applying the 0-1 test using other method

N_small=500;
N_large=5500;
N=N_large-N_small;
N_c=1000;
c=linspace(0,2*pi,N_c);
j=linspace(1,N_large,N_large);

for i=1:N_c
    for n=1:N_large
        p_c(n,i)=cos(j(1:n)*c(i))*x(1:n);
        q_c(n,i)=sin(j(1:n)*c(i))*x(1:n);
    end
end

M_c(1:N_small,1:N_c)=0;

for i=1:N_c
    for n=1:N_small
        for k=1:N
            M_c(n,i)=M_c(n,i)+ 1/N*((p_c(n+k,i)-p_c(k,i))^2+(q_c(n+k,i)-q_c(k,i))^2);
        end
    end
end

E_phi=0;
for i=1:N
    E_phi=E_phi+1/N*x(i);
end

```

```

end

for n=1:N_small
    for i=1:N_c
        V_osc(n,i)=E_phi^2*(1-cos(n*c(i)))/(1-cos(c(i)));
    end
end

D_c=M_c-V_osc;

%% regressing method
% D_c_til=D_c-min(min(D_c));
% K_c= log(D_c_til(1500,:))/log(N_small);

%% correlation method
x_bar(1:N_c)=0;
y_bar=0;
for i=1:N_c
    for j=1:N_small
        x_bar(i)=x_bar(i)+D_c(j,i);
    end
end
for j=1:N_small
    y_bar=y_bar+j;
end

x_bar=x_bar/N_small;
y_bar=y_bar/N_small;

cov(1,1:N_c)=0;
var_D(1,1:N_c)=0;
var_y(1,1:N_c)=0;

for i=1:N_c

```



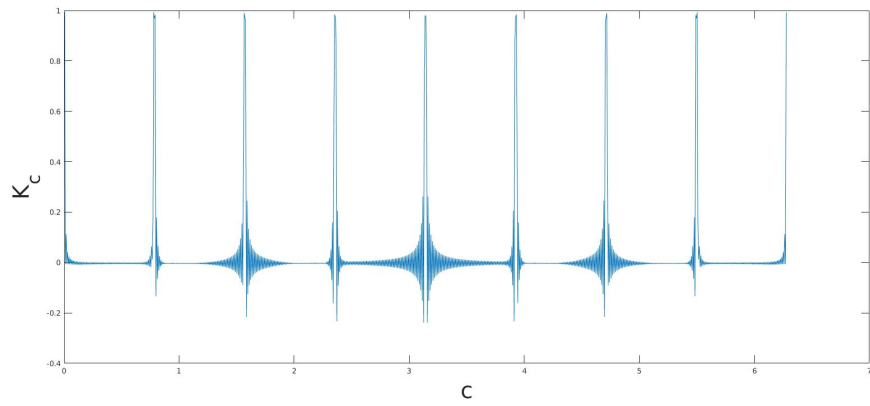
```

    for j=1:N_small
        cov(i)=cov(i)+1/N_small*(D_c(j,i)-x_bar(i))*(j-y_bar);
    end
end
for i=1:N_c
    for j=1:N_small
        var_D(i)=var_D(i)+1/N_small*(D_c(j,i)-x_bar(i))*(D_c(j,i)-x_bar(i));
        var_y(i)= var_y(i)+1/N_small*(j-y_bar)*(j-y_bar);
    end
end

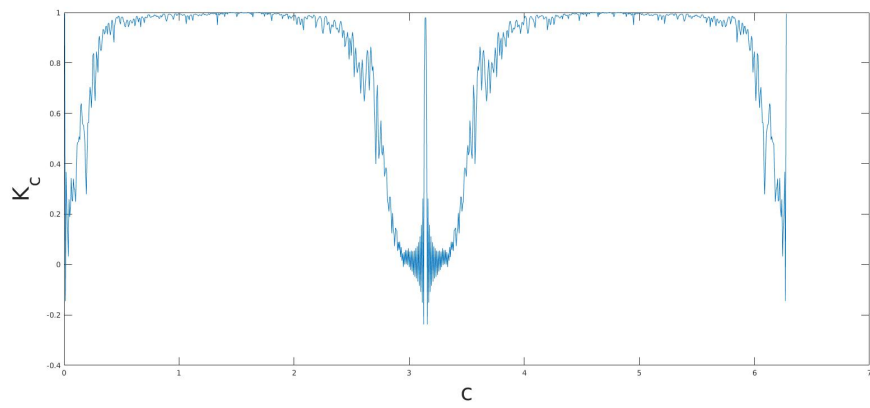
for i=1:N_c
K_c(i)=cov(i)/(var_D(i)*var_y(i))^0.5;
end

plot(c,K_c)
xlabel ('c')
ylabel ('K_c')

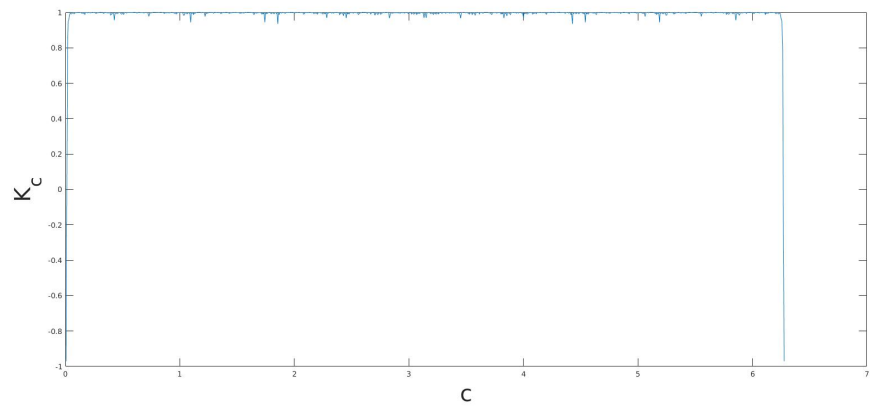
```



(a)



(b)



(c)

Figure 7.1: Plot of K_c vs c for logistic map with μ equal to (a) 3.55, (b) 3.6 and (c) 3.9

References

- [1] H. G. Weller, G. Tabor, H. Jasak, and C. Fureby. A tensorial approach to computational continuum mechanics using object-oriented techniques. *Computers in physics* 12, (1998) 620–631.
- [2] O. N. Griffin and S. E. Ramberg. Vortex shedding from a cylinder vibrating in line with an incident uniform flow. *J. Fluid Mech.* 75, (1976) 257.
- [3] A. Okajima. Strouhal numbers of rectangular cylinders. *J. Fluid Mech.* 123, (1982) 379.
- [4] C. Barbi, D. P. Favier, C. A. Maresca, and D. P. Telionis. Vortex shedding and lock-on of a circular cylinder in oscillatory flow. *J. Fluid Mech* 170, (1986) 527.
- [5] A. Ongoren and D. Rockwell. Flow structure from an oscillating cylinder Part 2. Mode competition in the near wake. *J. Fluid Mech* 191, (1988) 225.
- [6] S. J. Xu, Y. Zhou, and M. H. Wang. A symmetric binary-vortex street behind a longitudinally oscillating cylinder. *J. Fluid Mech.* 556, (2006) 27.
- [7] E. Konstantinidis and S. Balabani. Symmetric vortex shedding in the near wake of a circular cylinder due to streamwise perturbations. *J. Fluids Structures* 23, (2007) 1047.
- [8] E. Detemple-Laake and H. Eckelmann. Phenomenology of Kármán vortex streets in oscillatory flow. *Exp. Fluids* 7, (1989) 217.

- [9] C. Y. Zhou and J. M. R. Graham. A numerical study of cylinders in waves and currents. *J. Fluids Structures* 14, (2000) 403.
- [10] T. Srikanth, H. N. Dixit, R. Tataavarti, and R. Govindarajan. Vortex shedding patterns, their competition, and chaos in flow past inline oscillating rectangular cylinders. *Phys. Fluids* 23, (2011) 073,603 (1–9).
- [11] H. A. Khaledi, H. I. Andersson, M. Barri, , and B. Pettersen. Flow past a normal flat plate undergoing inline oscillations. *Phys. Fluids* 24, (2012) 093,603.
- [12] G. Vittori and P. Blondeaux. Quasiperiodicity and phase locking route to chaos in 2-D oscillatory flow around a circular cylinder. *Phys. Fluids A* 5(8), (1993) 1866.
- [13] P. G. Perdikaris, L. Kaiktsis, and G. S. Triantafyllou. Chaos in a cylinder wake due to forcing at the Strouhal frequency. *Phys. Fluids* 21, (2009) 101,705.
- [14] G.-H. Cottet and P. D. Koumoutsakos. Vortex methods: theory and practice. Cambridge University Press, 2000.
- [15] C. Von Kerczek and S. H. Davis. Linear stability theory of oscillatory Stokes layers. *Journal of Fluid Mechanics* 62, (1974) 753–773.
- [16] C. E. Grosch and H. Salwen. The stability of steady and time-dependent plane Poiseuille flow. *Journal of Fluid Mechanics* 34, (1968) 177–205.
- [17] S. Mineswitsch, R. Franke, and W. Rodi. Numerical investigation of laminar vortex-shedding flow past a square cylinder oscillating in line with the mean flow. *J. Fluids Struct.* 8, (1994) 787.
- [18] S. Ansumali, S. S. Chikatamarla, C. E. Frouzakis, and K. Boulouchos. Entropic Lattice Boltzmann Simulation of the Flow Past Square Cylinder. *Int. J. Mod. Phys. C* 15(3), (2004) 435.
- [19] G. A. Gottwald and I. Melbourne. A new test for chaos in deterministic systems. In *Proceedings of the Royal Society of London A: Mathematical, Physical and Engineering Sciences*, volume 460. The Royal Society, 2004 603–611.

- [20] G. A. Gottwald and I. Melbourne. On the implementation of the 0-1 test for chaos. *SIAM Journal on Applied Dynamical Systems* 8, (2009) 129–145.
- [21] L. S. Hultgren and A. K. Aggarwal. Absolute instability of the Gaussian wake profile. *Phys. Fluids* 30, (1987) 3383–3387.